RSC Advances

PAPER

View Article Online
View Journal | View Issue

Cite this: *RSC Adv.*, 2026, **16**, 21833

First-principles study of lead-free A_3InX_6 (A = Rb, Cs; X = Cl, Br, I) defect -perovskites: structural, electronic, optical, and mechanical properties

Rifat Rafiu,[a] Md. Sakib Hasan,[a] Imtiaz Ahamed Apon,[b] Md. Azizur Rahman,*[c] Mohamed Benghanem,*[d] Amnah Mohammed Alsuhaibani,[e] Moamen S. Refat[f] and Noureddine Elboughdiri[g]

The development of environmentally benign and stable alternatives to lead-based perovskites remains a key challenge for next-generation photovoltaic materials. In this work, a comprehensive first-principles investigation of lead-free alkali indium halide defect-perovskites A_3InX_6 (A = Rb, Cs; X = Cl, Br, I) is performed to elucidate the influence of cation and anion substitution on their structural, electronic, optical, and mechanical properties. Density functional theory calculations using GGA-PBE and PBEsol functionals confirm that all compositions crystallize in a stable cubic phase with negative formation energies and favorable Goldschmidt tolerance factors, where substitution of the larger Cs^+ cation enhances lattice stability compared to Rb^+. Systematic halide substitution from Cl^- to Br^- to I^- induces lattice expansion and a pronounced reduction in the direct band gap at the Γ-point, enabling effective band gap tunability. Electronic structure analysis reveals that the valence-band maximum is dominated by halogen p states, while the conduction band is primarily governed by In-derived states, underscoring the decisive role of anion chemistry in controlling electronic transitions. Optical calculations demonstrate enhanced dielectric response and significantly improved visible-light absorption for iodide-rich compositions, whereas chloride-based compounds retain wide band gaps and stronger structural rigidity. Mechanical and elastic analyses indicate that both cation and anion substitution modulate lattice stiffness, ductility, and hardness, with Cs- and I-based compounds exhibiting increased mechanical softness and improved machinability.

Received 19th January 2026
Accepted 20th April 2026

DOI: 10.1039/d6ra00473c

rsc.li/rsc-advances

1. Introduction

The advent of organic–inorganic hybrid halide perovskites, notably $CH_3NH_3PbI_3$, has catalyzed a revolution in photovoltaics, with certified power conversion efficiencies (PCEs) soaring from 3.8% to over 25% within a decade.[1–4] This remarkable progress is attributed to their exceptional optoelectronic properties, including high absorption coefficients, ambipolar charge transport, long carrier diffusion lengths, and tunable band gaps, all achievable *via* low-temperature, solution-processable fabrication.[5,6] However, the path to commercialization is obstructed by two formidable challenges: the inherent instability of these materials under environmental stressors like moisture, heat, and light, and the toxicity of water-soluble lead (Pb^{2+}), which raises significant environmental and health concerns.[7,8]

The quest for lead-free alternatives has led researchers to explore isoelectronic elements. While tin (Sn^{2+}) was an initial candidate due to its similar electronic configuration, its propensity to rapidly oxidize from Sn^{2+} to Sn^{4+} under ambient conditions results in severe device instability, often making it less stable than its lead counterparts.[9,10] This has shifted focus towards trivalent cations, particularly antimony (Sb^{3+}) and bismuth (Bi^{3+}), which form stable, non-toxic compounds with the general formulae $A_3B_2X_9$ and A_3BX_6 (A = MA^+, Cs^+, Ag^+; B = Sb^{3+}, Bi^{3+}).[11–13] As demonstrated in the provided research, materials like $AgBi_2I_7$, $Cs_3Bi_2I_9$, and Ag_3BiI_6 have shown promising air stability and PCEs up to 4.3%.[14–16] However, these materials often suffer from fundamental limitations such as wide, indirect band gaps, high exciton binding energies, low electronic dimensionality, and poor charge carrier mobility,

[a]*Department of Material Science and Engineering, Khulna University of Engineering & Technology (KUET), Khulna - 9203, Bangladesh*

[b]*Electronics and Information Technology, University of South Wales, Treforest, Pontypridd, CF37 1DL, UK*

[c]*Department of Electrical and Electronic Engineering, Begum Rokeya University, Rangpur, 5400, Bangladesh. E-mail: azizurrahmanatik49@gmail.com*

[d]*Department of Physics, Faculty of Science, Islamic University of Madinah, Madinah 42351, Saudi Arabia. E-mail: mbenghanem@iu.edu.sa*

[e]*Department of Sports Health, College of Sport Sciences & Physical Activity, Princess Nourah bint Abdulrahman University, P.O. Box 84428, Riyadh 11671, Saudi Arabia*

[f]*Department of Chemistry, College of Science, Taif University, P.O. Box 11099, Taif 21944, Saudi Arabia*

[g]*Chemical Engineering Department, College of Engineering, University of Ha'il, P.O. Box 2440, 81441, Ha'il, Saudi Arabia*

which intrinsically cap their photovoltaic performance.[17,18] Furthermore, studies on Ag_3BiI_6 reveal unique degradation mechanisms driven by concerted ion migration (Ag^+, Bi^{3+}, I^-) and low decomposition enthalpy, leading to phase segregation and electrode corrosion, underscoring the complex stability challenges even in lead-free systems.[19]

In this landscape, indium (In^{3+})-based perovskites with the A_3InX_6 (A = Rb, Cs; X = Cl, Br, I) structure emerge as a compelling yet relatively unexplored class of lead-free candidates. Indium shares a stable trivalent state and possesses an electronic configuration ([Kr] $4d^{10}$ $5s^2$) that is conducive to forming semiconductors with desirable optoelectronic properties. The A_3InX_6 structure, often crystallizing in a vacancy-ordered double perovskite or related elpasolite structure, offers several potential advantages. The bandgap can be effectively engineered through halide alloying (Cl, Br, I), allowing for optimization of light absorption across the solar spectrum. The all-inorganic composition (using Cs^+ or Rb^+) eliminates volatile organic cations, potentially enhancing thermal and structural stability compared to hybrid perovskites. Preliminary theoretical studies suggest that certain vacancy-ordered perovskites can exhibit good defect tolerance, which is crucial for achieving high open-circuit voltages (V_{OC}).[18] Compared to the fast migration of small Ag^+ ions observed in rudorffites like Ag_3BiI_6,[20] the larger ionic radii of Rb^+, Cs^+, and In^{3+} may intrinsically suppress detrimental ion migration, a key factor for operational stability and reduced hysteresis. Despite this promise, the development of A_3InX_6 perovskites for photovoltaics is still in its infancy. A_3InX_6, where A is a Group-1 monovalent cation (Rb^+ or Cs^+), and X is a halide anion (Cl^-, Br^-, I^-). Their typically wider band gaps (>2 eV for most compositions) may limit their use as single-junction absorbers but make them excellent candidates for tandem cell top cells or UV-selective photodetectors. The challenges lie in mastering thin-film processing to achieve dense, pinhole-free layers with high crystallinity and in designing optimal device architectures that facilitate efficient charge extraction from these materials.[21–23]

Despite the remarkable progress of halide perovskites in optoelectronic research, the presence of toxic lead and the limited long-term stability of many existing compositions continue to impede their sustainable deployment. While several lead-free alternatives based on trivalent cations such as Bi^{3+} and Sb^{3+} have been explored, these materials often suffer from intrinsic drawbacks, including wide or indirect band gaps, reduced charge-transport characteristics, and limited optical absorption in the visible region.[24] Consequently, identifying new lead-free perovskite-derived materials with favorable electronic structure, strong light–matter interaction, and robust structural stability remains a critical challenge. In this context, alkali-indium halide defect-perovskites A_3InX_6 (A = Rb, Cs; X = Cl, Br, I) represent a largely unexplored material family with significant potential for optoelectronic applications. The stable trivalent oxidation state of indium, combined with the all-inorganic nature of these compounds, offers prospects for improved chemical and structural stability compared to hybrid perovskites. Moreover, the availability of both A-site cation substitution (Rb^+/Cs^+) and halide anion substitution (Cl^-/Br^-/I^-) provides an effective route for systematically tuning lattice geometry, electronic band structure, and optical response.

However, a comprehensive understanding of how cation and anion substitution collectively influence the structural, electronic, optical, and mechanical properties of A_3InX_6 defect-perovskites is still lacking. In particular, detailed insights into band-gap tunability, orbital contributions near the band edges, optical absorption behavior across the infrared to ultraviolet regions, and mechanical robustness are essential to assess the suitability of these materials for future optoelectronic technologies. Motivated by this gap, the present study employs first-principles density functional theory calculations to establish clear structure–property relationships in A_3InX_6 compounds, providing a systematic theoretical foundation to guide future experimental synthesis and materials optimization.

2. Computational method

2.1. Material Studio-based DFT methodology

The physical properties, including structural, electronic, optical, mechanical, elastic anisotropy, charge density distribution, and population characteristics, of A_3InX_6 (A = Rb, Cs; X = Cl, Br, I) halide double perovskites were systematically investigated using first-principles calculations based on Density Functional Theory (DFT), as implemented in the CASTEP package.[25,26] This *ab initio* approach provides a reliable and predictive framework for exploring the structural stability and physicochemical behavior of crystalline solids. Geometry optimization and property calculations were performed using the generalized gradient approximation (GGA) with the Perdew–Burke–Ernzerhof (PBE) exchange-correlation functional, while the Generalized Gradient Approximation PBE revised for solids (GGA-PBEsol) was employed to validate the electronic structure and accurately estimate the band gaps.[27–30] Ultrasoft Vanderbilt-type pseudopotentials were adopted for Rb, Cs, In, Cl, Br, and I atoms to efficiently and accurately describe the electron–ion interactions. A plane-wave cutoff energy of 700 eV was selected to ensure total-energy convergence and precise electronic state representation.[31–33] The Brillouin zone was sampled with a Monkhorst–Pack *k*-point mesh of 8 × 8 × 8, guaranteeing reliable convergence for total energy, stress, and force calculations across reciprocal space.[34,35] X-ray diffraction (XRD) patterns were simulated using the Forcite module to analyze the diffraction behavior of the optimized structures and to verify the consistency of the adopted crystallographic models.[36] Structural optimizations were performed under strict convergence criteria, including a maximum energy difference of 1.0×10^{-6} eV per atom, a maximum force of 0.006 eV $Å^{-1}$, a maximum displacement of 2.0×10^{-4} Å, and a maximum stress tolerance of 0.02 GPa.[37] The electronic configurations considered in the calculations correspond to the valence states of each element: Rb and Cs with closed-shell p orbitals and a single outer s electron; In with a fully occupied d shell along with s and p valence electrons; and halogen atoms (Cl, Br, and I) with filled s orbitals and partially filled p orbitals. The optical properties, including the complex dielectric function, absorption coefficient, refractive index, reflectivity, and optical conductivity,

were derived from the frequency-dependent dielectric response based on interband electronic transitions. The mechanical properties were evaluated through the calculated elastic constants, from which bulk modulus, shear modulus, Young's modulus, Poisson's ratio, and Vickers hardness were derived to assess mechanical stability and ductility. The graphical visualization of the elastic properties was generated using an open-source computational framework based on the ELATE methodology. The elastic tensor components obtained from first-principles calculations were used as input to evaluate the directional dependence of the elastic moduli. The corresponding ELATE-based formulations were implemented within a Python-based environment to compute and visualize the anisotropic elastic behavior. This approach enables the calculation and representation of both three-dimensional and two-dimensional projections of the elastic parameters, providing insight into the anisotropy of the materials. The use of an open and script-based computational workflow ensures transparency and reproducibility of the elastic property analysis presented in this study. The charge density distribution and charge density difference maps were analyzed to elucidate bonding characteristics and charge transfer between constituent atoms. Finally, population analysis, including Mulliken charges and bond populations, was performed to quantify the ionic-covalent nature of chemical bonding in A_3InX_6 double perovskite compounds.

3. Material Studio-based results and discussion

3.1. Optimized structural properties

The metal halide perovskite A_3InX_6 in this research exhibits a crystal structure that possesses the space group $Fm\bar{3}m$ (225). As illustrated in Fig. 1, the sites 8c and 4b, 4a, and 24e are occupied by Cs/Rb, In, and halide (Cl/Br/I) atoms, respectively. This structural assignment is supported by recent theoretical and experimental studies on similar halide perovskites, where compounds with analogous compositions have been reported to stabilize in the cubic $Fm\bar{3}m$ phase. For instance, A_3GaI_6 (A = Cs, K, and Rb) has been demonstrated to adopt a stable cubic structure within the same space group.[38] Similarly, recent work such as "Efficient Discovery of Lead-Free A_3BX_3 Halide Perovskites *via* Machine Learning" also predicts the stability of cubic $Fm\bar{3}m$ phases for related compounds.[39] Although alternative structural configurations (*e.g.*, lower-symmetry phases) have been reported in some cases,[40] the present cubic model is considered a reasonable and physically justified approximation for describing the structural and electronic properties of the studied system.

The optimized Cartesian coordinates are given in Tables S1 and S2. Tables 1 and S3 summarize the calculated structural and electronic properties of the investigated halide perovskites using different exchange-correlation functionals, together with previously reported theoretical and experimental data for related compounds reported in the literature.[40–42] As summarized in Table 1, the lattice constant and unit cell volume increase systematically with the halide ionic radius, following the order Cl < Br < I. For instance, the lattice constant expands from 8.026 Å (Rb_3InCl_6) to 9.247 Å (Rb_3InI_6), while the corresponding unit cell volume rises from 365.666 Å3 to 559.137 $Å^3$. A similar trend is observed for Cs-based perovskites, where Cs substitution results in larger lattice expansion compared to Rb due to the higher ionic radius of Cs^+. Although the unit cell volume increases from Cl to Br to I due to the larger ionic radii of the halide ions, the density increases across the series. This is because the significant increase in atomic mass from Cl to Br to I outweighs the effect of lattice expansion. The electronic band gap shows the opposite trend, decreasing from Cl to I (*e.g.*, Rb_3InCl_6: 3.515 eV → Rb_3InI_6: 1.335 eV), which originates from

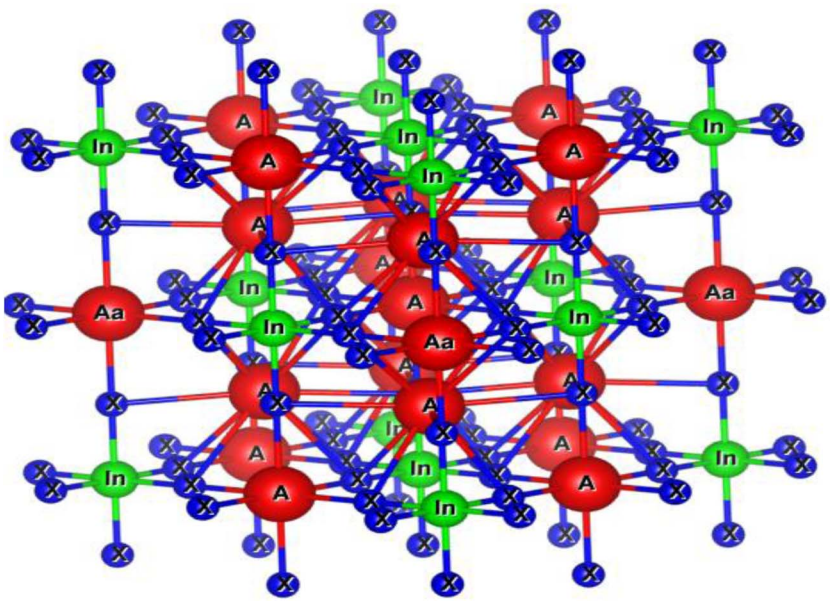

Fig. 1 The crystal structure of A_3InX_6 (A = Rb, Cs, and X = Cl, Br, I) defect-perovskites materials.

Table 1 The energy band gap, lattice constants, unit cell volume, and formation enthalpy of A_3InX_6 (A = Rb, Cs, and X = Cl, Br, I) perovskites calculated using the GGA-PBE functional

Compounds	Band gaps (E_g)	Lattice constant a (Å)	Unit cell volume, V (Å^3)	Density (g cm^{-3})	Formation energy, ΔE_f (eV per atom)
Rb_3InCl_6	3.515	8.026	365.666	2.651	−3.318
Rb_3InBr_6	2.440	8.468	429.431	3.289	−2.957
Rb_3InI_6	1.335	9.247	559.137	3.363	−2.564
Cs_3InCl_6	3.567	8.297	403.973	2.985	−3.338
Cs_3InBr_6	2.570	8.706	466.654	3.533	−2.989
Cs_3InI_6	1.430	9.433	593.578	3.566	−2.610

enhanced orbital overlap and narrowing of the conduction-valence band separation in heavier halides.

Additionally, formation energy (ΔE_f) is a fundamental thermodynamic quantity that measures the energetic stability of a compound relative to its constituent elements in their standard states. It is defined as the difference between the total energy of the compound and the weighted sum of the energies of the isolated elemental phases, normalized per atom.[43] A negative ΔE_f indicates that the compound forms exothermically and is thermodynamically stable, while more negative values imply stronger bonding and higher resistance to decomposition.[43] The formation enthalpy (ΔE_f) of A_3InX_6 was calculated using the total energy obtained from the optimized crystal structure. The reference energies of the constituent elements were taken from their standard states, where A and In correspond to their bulk phases and the halogen X was evaluated as $\frac{1}{2}E(X_2)$ for the diatomic gas molecules (*e.g.*, $\frac{1}{2}E(Cl_2)$, $\frac{1}{2}E(Br_2)$, or $\frac{1}{2}E(I_2)$),

$$\Delta H_f = E_{tot}(A_3InX_6) - 3E(A) - E(In) - 6E(X) \quad (1)$$

Tables 1 and S1 summarize the calculated formation energies of the alkali-indium halide defect-perovskites Rb_3InX_6 and Cs_3InX_6 (X = Cl, Br, I). All compounds exhibit negative formation energies (from −3.338 to −2.564 eV per atom), confirming their intrinsic thermodynamic stability and feasibility for experimental synthesis. For both Rb- and Cs-based series, ΔE_f becomes less negative when moving from Cl → Br → I. This systematic trend reflects the increasing ionic radius and decreasing electronegativity of the halogen anions, which weakens the In–X bonding strength and slightly reduces lattice stability. Comparing the A-site cations, the Cs_3InX_6 compounds show marginally more negative ΔE_f than their Rb_3InX_6 counterparts for the same halogen, indicating that the larger Cs^+ ion provides better lattice stabilization in these cubic defect-perovskite frameworks. Overall, the formation-energy analysis in Table 1 demonstrates that all investigated compounds are thermodynamically stable, with chloride-based compositions being the most stable and iodide-based compositions the least stable within each alkali series.

The Goldschmidt tolerance factor (t) is a widely used geometric criterion to evaluate the structural stability and symmetry of perovskite and defect-perovskite materials.[44,45] The tolerance factor of a given compound can be evaluated using the following equation,

$$t = \frac{(r_A + r_X)}{\sqrt{2}(r_{In} + r_X)} \quad (2)$$

In general, a tolerance factor in the range $0.8 \leq t \leq 1.0$ indicates a stable cubic or near-cubic structure, whereas values significantly lower or higher than this range may lead to octahedral tilting, lattice distortion, or lower-symmetry phases.[46,47]

Table 2 lists the calculated tolerance factors for the alkali-indium halide defect-perovskites Rb_3InX_6 and Cs_3InX_6 (X = Cl, Br, I). All compounds exhibit values between 0.924 and 1.000, which fall within the acceptable stability window, confirming their geometric compatibility with the cubic defect-perovskite structure.

For both alkali series, the tolerance factor decreases systematically from Cl → Br → I, reflecting the increase in halide ionic radius that slightly distorts the lattice and reduces structural compactness. Comparing the A-site cations, the Cs-based compounds consistently show higher t values than the corresponding Rb analogues due to the larger ionic radius of Cs^+. Notably, Cs_3InCl_6 ($t = 1.000$) represents an ideal geometric match, suggesting a highly stable and nearly perfect cubic framework. Overall, the tolerance-factor analysis in Table 2 indicates that all investigated compounds possess favorable geometric stability, with Cs_3InCl_6 being the most structurally ideal and iodide-based compositions showing slightly increased lattice distortion while remaining within the stable regime.

3.2. X-ray diffraction (XRD) analysis

X-ray diffraction (XRD) analysis was used to examine the structural characteristics of the optimized compounds. The diffraction peak positions were determined according to Bragg's law,[48] which relates the diffraction angle to the interplanar spacing of the crystal lattice.[49] Detailed expressions (eqn (S1)

Table 2 Tolerance factor variation in A_3InX_6 (A = Rb, Cs, and X = Cl, Br, I) defect-perovskites

Materials	r_A	r_{In}	r_X	Tolerance factor (t)
Rb_3InCl_6	1.72	0.80	1.81	0.956
Rb_3InBr_6	1.72	0.80	1.96	0.943
Rb_3InI_6	1.72	0.80	2.20	0.924
Cs_3InCl_6	1.88	0.80	1.81	1.000
Cs_3InBr_6	1.88	0.80	1.96	0.984
Cs_3InI_6	1.88	0.80	2.20	0.961

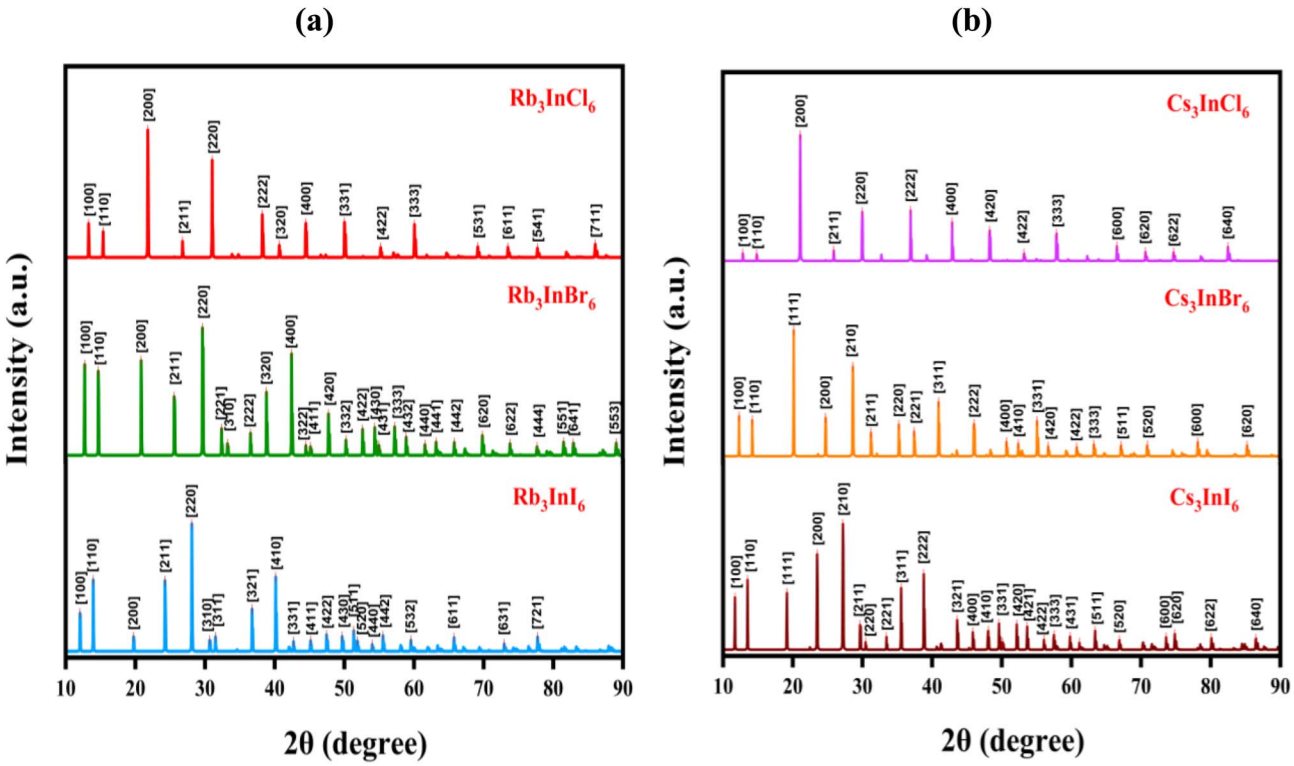

Fig. 2 Calculated X-ray diffraction spectra of (a) Rb_3InX_6 and (b) Cs_3InX_6 of double perovskite materials.

and (S2)) used in the calculations are provided in the SI. Fig. 2 presents the calculated X-ray diffraction (XRD) patterns of double perovskite compounds with the general formula A_3InX_6, where A = Rb or Cs and X = I, Br, or Cl. The diffraction intensity is plotted as a function of the Bragg angle (2θ) over a range of approximately 10° to 90°. The cubic $Fm\bar{3}m$ structure (Materials Project mp-1110693) was selected as a high-symmetry reference model to enable consistent comparison across the A_3InX_6 series.[50] For the Rb-based compounds in Fig. 2(a), the simulated diffraction profiles exhibit multiple reflections corresponding to characteristic crystallographic planes over a wide 2θ range (10°–90°). The main low-angle peaks appear at approximately 12–13° (111), 15–16° (200), 20–22° (220), 24–26° (311), 28–30° (222), 31–33° (400), 36–38° (331), and 39–41° (420). In addition to these major reflections, several higher-angle peaks are observed, including (422), (511), (531), (600), and other higher-index planes, consistent with the cubic symmetry of the adopted model. Among the reflections, the (220) and (222) peaks exhibit relatively higher intensity. A systematic shift of peak positions toward higher 2θ values is observed when moving from Rb_3InI_6 to Rb_3InBr_6 and Rb_3InCl_6, which is consistent with the reduction in lattice spacing associated with the decreasing ionic radius from I^- to Br^- to Cl^-. Fig. 2(b) shows the calculated patterns for the Cs-based compounds, where similar reflection sequences are observed across the full 2θ range. The principal peaks appear at approximately 11–12° (111), 14–15° (200), 19–21° (220), 24–26° (311), 27–29° (222), 30–32° (400), 34–36° (331), 36–38° (420), and 40–41° (422). Additional higher-angle reflections such as (511), (600), (620), and related planes are also clearly visible, indicating consistent indexing across the diffraction pattern. Compared with the Rb-based systems, the peaks for Cs compounds are systematically shifted toward lower 2θ values, which is consistent with the larger ionic radius of Cs^+ and the corresponding expansion of lattice parameters. All major reflections across the full 2θ range can be consistently indexed based on the reflection conditions of the cubic $Fm\bar{3}m$ space group, supporting internal consistency of the adopted structural model. These simulated diffraction profiles are consistent with structural variations differences that arise from both halide substitution and A-site cation size.[51,52]

It should be noted that the cubic $Fm3m$ structure employed in this work represents a high-symmetry reference model adopted to enable systematic comparison across the A_3InX_6 compositional series. Similar group materials, such as Q_3GaBr_6 (Q = K and Na), have also been reported to exhibit cubic structures with $Fm\bar{3}m$ symmetry based on simulated XRD analysis.[41] Importantly, previous experimental studies have reported lower-symmetry phases for related compounds, such as the monoclinic $C2/c$ structure for Rb_3InCl_6.[40] Such variations may arise from differences in synthesis conditions, temperature effects, or structural distortions. In the absence of comprehensive comparative stability analysis across competing phases, the cubic $Fm\bar{3}m$ phase is adopted here as a consistent and physically reasonable reference model for systematic investigation. It is further emphasized that simulated XRD patterns reflect the diffraction response of optimized structural models and cannot independently confirm phase purity or exclude competing polymorphs. In addition, simulated peak intensities depend on normalization and peak-broadening parameters and do not capture experimental effects such as crystallite size,

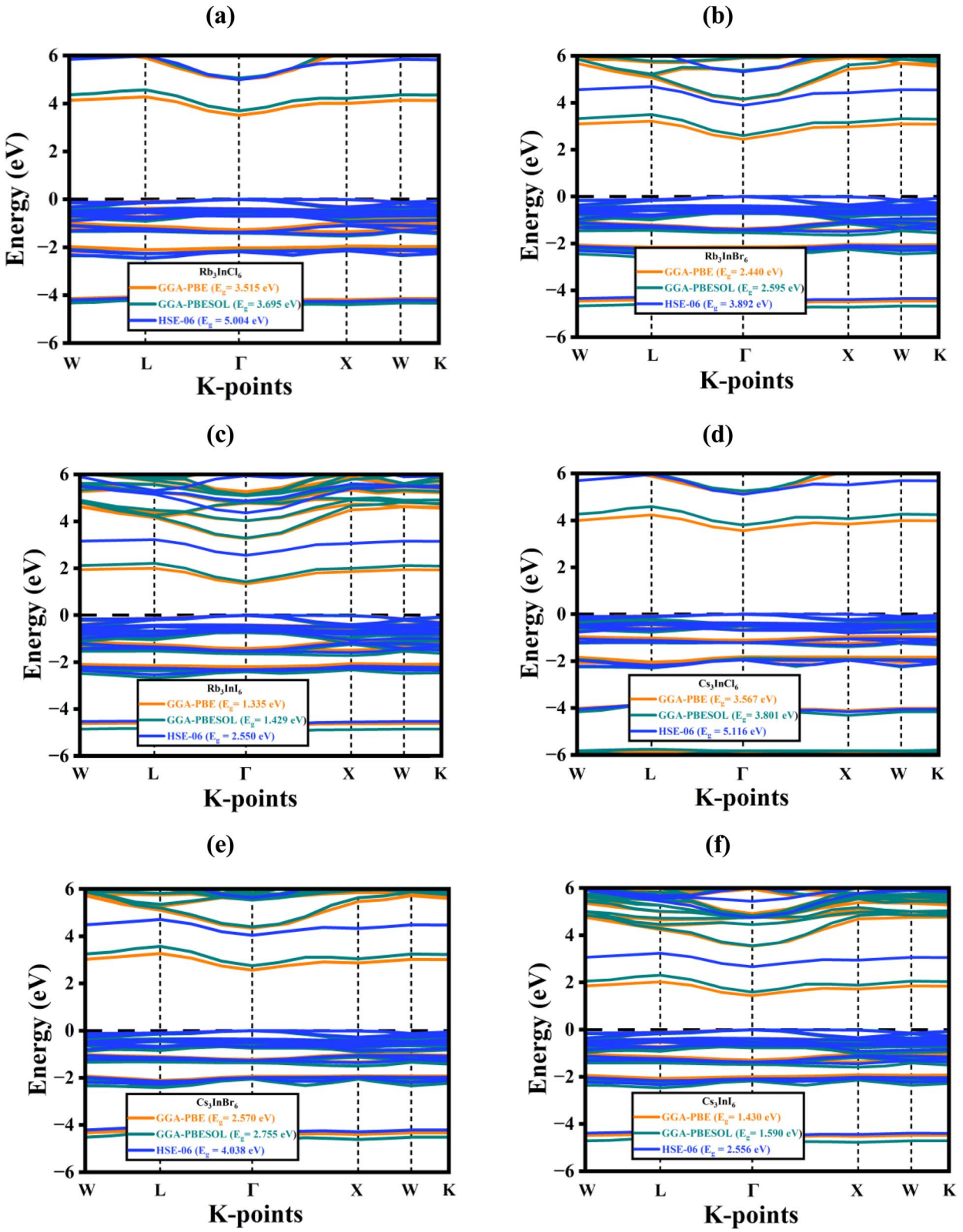

Fig. 3 Electronic band structures of (a) Rb_3InCl_6, (b) Rb_3InBr_6, (c) Rb_3InI_6, (d) Cs_3InCl_6, (e) Cs_3InBr_6, and (f) Cs_3InI_6 calculated using the GGA-PBE and GGA-PBEsol exchange-correlation functionals.

strain, preferred orientation, or defects. A rigorous determination of the ground-state crystal symmetry would require comparative total-energy calculations of candidate structures along with high-resolution experimental diffraction analysis using quantitative refinement methods such as Rietveld fitting, which is beyond the scope of the present study.

3.3. Electronic properties

The electronic band structures of the investigated materials were calculated within the framework of density functional theory (DFT) using the GGA-PBE, GGA-PBEsol, and hybrid HSE06 exchange-correlation functionals. The GGA-PBE functional is widely adopted owing to its computational efficiency, reasonable accuracy, and low computational cost, which makes it suitable for the systematic evaluation of electronic, optical, and other related physical properties using modest computational resources. The GGA-PBEsol functional, a revised version of PBE for solid-state systems, generally provides improved equilibrium structural properties and slightly larger bandgap values.[53,54] For a more reliable description of the electronic structure, particularly the bandgap, the screened hybrid functional HSE06 was additionally employed,[55] as hybrid functionals are known to reduce the bandgap underestimation typically observed in semi local GGA approaches.[56–58]

As shown in Fig. 3(a)–(f), all compounds exhibit a direct bandgap, with both the valence band maximum (VBM) and conduction band minimum (CBM) located at the Γ point of the Brillouin zone (W–L–Γ–X–W–K), which is favorable for optoelectronic and photovoltaic applications. The calculated bandgap values for Rb_3InCl_6, Rb_3InBr_6, and Rb_3InI_6 are 3.515, 2.440, and 1.335 eV using GGA-PBE, and 3.695, 2.595, and 1.429 eV using GGA-PBEsol, respectively, while the HSE06 functional predicts larger bandgaps of 5.004, 3.892, and 2.550 eV for the same compounds. Similarly, Cs_3InCl_6, Cs_3InBr_6, and Cs_3InI_6 exhibit bandgaps of 3.567, 2.570, and 1.430 eV with GGA-PBE, which increase to 3.801, 2.755, and 1.590 eV when calculated using GGA-PBEsol, while the HSE06 functional further increases the bandgaps to 5.116, 4.038, and 2.556 eV, respectively. For both Rb- and Cs-based compounds, the bandgap decreases systematically from Cl to Br to I, which can be attributed to the increasing halide ionic radius and the enhanced contribution of halogen p states near the valence band edge.[51–53] In all cases, the HSE06 hybrid functional yields significantly larger bandgaps due to the inclusion of a portion of exact exchange, which reduces the typical bandgap underestimation of semi local GGA functionals.

Importantly, Rb_3InI_6 and Cs_3InI_6 possess bandgaps within the optimal photovoltaic bandgap of 1.0–1.80 eV,[59] combined with a direct bandgap nature. These features indicate that the iodide-based compounds are particularly promising candidates for solar cell applications, whereas the chloride- and bromide-based materials are more suitable for wide-bandgap optoelectronic devices.

The partial density of states (PDOS) and total density of states (TDOS) were analyzed to gain a comprehensive understanding of the orbital-resolved electronic structure and to validate the band-structure results. The TDOS profiles clearly exhibit a finite bandgap for all investigated compounds, with no electronic states crossing the Fermi level (set at 0 eV), confirming their intrinsic semiconducting behavior. The valence band (V_B) edge lies just below the Fermi level, while the conduction band (C_B) edge starts just above it; the energy separation between these two edges defines the bandgap.[60,61] From the PDOS analysis, the upper valence band region is mainly governed by the halogen p orbitals, namely Cl-3p, Br-4p, and I-5p, with small but noticeable contributions from In-5s and In-5p states. This indicates that the valence band electronic states are primarily controlled by the halide sublattice. In contrast, the conduction band is dominated by In-5p states, with additional hybridization from the A-site alkali metal s orbitals (Rb-s or Cs-s). The alkali metal p orbitals contribute negligibly to both the valence and conduction bands, demonstrating that Rb and Cs ions mainly play a structural stabilization role rather than directly influencing the electronic transitions.

The TDOS maximum peak values at the VBM are calculated to be 30.74, 29.178, and 27.822 states per eV for Rb_3InCl_6, Rb_3InBr_6, and Rb_3InI_6, respectively, while Cs_3InCl_6, Cs_3InBr_6, and Cs_3InI_6 exhibit corresponding values of 32.318, 31.59, and 19.676 states per eV, as shown in Fig. 4. On the other hand, the maximum TDOS peaks at the CBM are 18.54, 19.676, and 22.189 states per eV for Rb_3InCl_6, Rb_3InBr_6, and Rb_3InI_6, respectively, and 17.786, 18.926, and 24.378 states per eV for Cs_3InCl_6, Cs_3InBr_6, and Cs_3InI_6, as shown in Fig. 4.

The extracted bandgap values from the TDOS are 3.515 eV, 2.440 eV, and 1.335 eV for Rb_3InCl_6, Rb_3InBr_6, and Rb_3InI_6, respectively, and 3.567 eV, 2.570 eV, and 1.430 eV for Cs_3InCl_6, Cs_3InBr_6, and Cs_3InI_6. These results are fully consistent with the band-structure calculations and show a systematic reduction of the bandgap from Cl → Br → I, originating from the increasing contribution of halogen p states near the valence band edge.[62] Overall, the combined PDOS and TDOS analyses confirm that the electronic properties of these materials are mainly dictated by In–X orbital interactions, while the alkali metal cations act as charge-balancing and lattice-stabilizing species. The favorable electronic features of the iodide-based compounds further support their suitability for photovoltaic and optoelectronic applications.

3.4. Optical properties

The optical properties of A_3InX_6 (A = Rb, Cs; X = Cl, Br, I) perovskites describe their interaction with electromagnetic radiation across the infrared, visible, and ultraviolet regions and are critical for optoelectronic and photovoltaic applications. Optical analysis provides key information on absorption edges, electronic transition mechanisms, dielectric response, optical conductivity, and refractive behavior. These parameters determine the efficiency of light absorption, charge-carrier generation, and interband transitions.[63] Comparing different halide compositions enables the identification of materials with optimal spectral coverage and strong light–matter interaction, supporting their potential use in solar cells, UV-visible photodetectors, LEDs, and laser devices.[64]

3.4.1. Absorption coefficient (α). Fig. 5(a) illustrates the absorption coefficient spectra of A_3InX_6 over the photon-energy range of 0–16 eV, encompassing the infrared (IR), visible, and ultraviolet (UV) regions.[65] It measures the attenuation of incident radiation per unit path length expressed in the eqn (S3). As shown in Fig. 5(a), absorption begins at 3.515 eV for Rb_3InCl_6, 2.440 eV for Rb_3InBr_6, and 1.335 eV for Rb_3InI_6, while the corresponding values

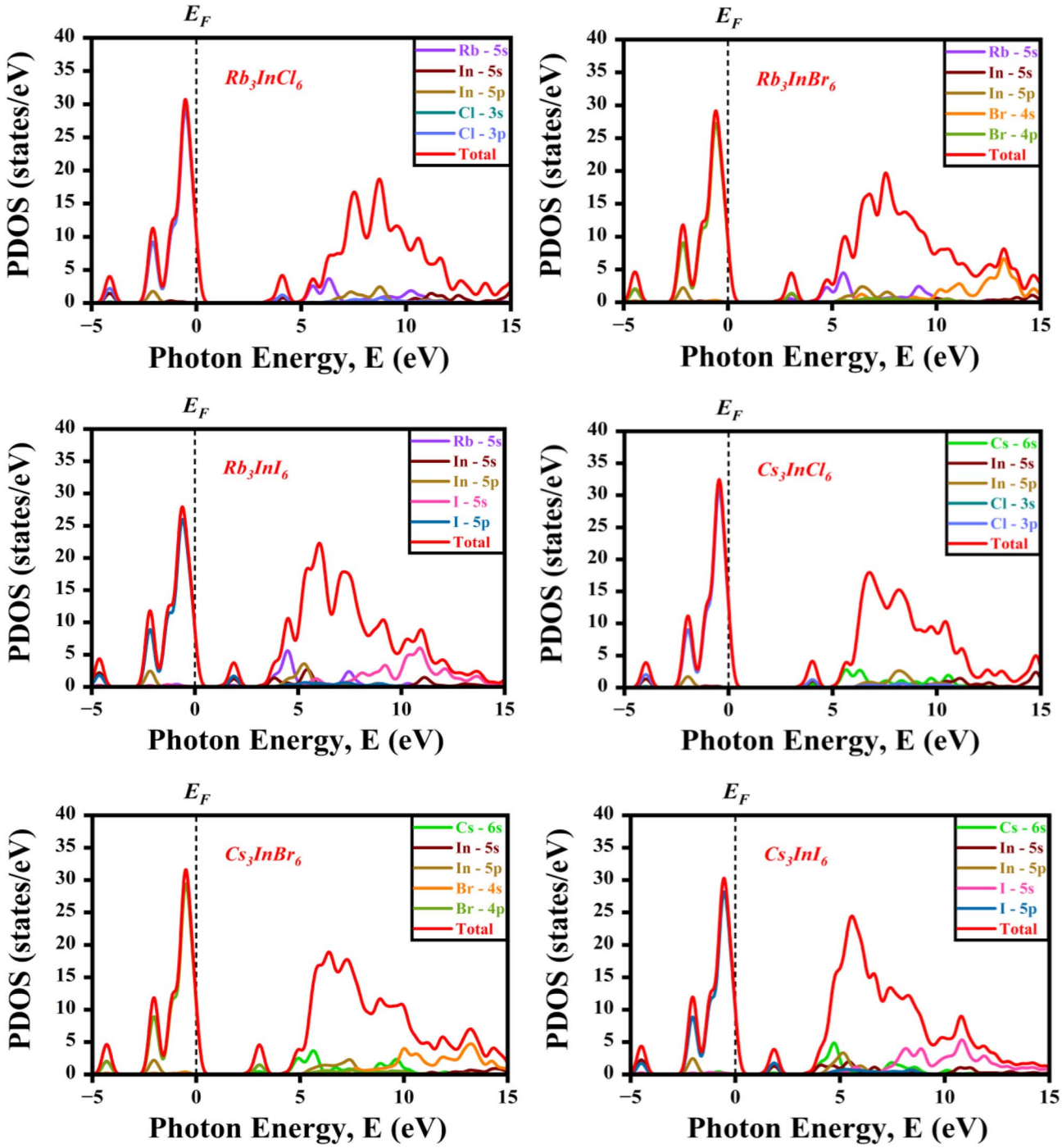

Fig. 4 The PDOS and TDOS of A_3InX_6 perovskite materials.

for the Cs-based compounds are 3.567 eV for Cs_3InCl_6, 2.570 eV for Cs_3InBr_6, and 1.430 eV for Cs_3InI_6. This systematic redshift from Cl to I reflects the reduction in bandgap with increasing halide ionic size. In the visible region, Fig. 5(a) shows negligible absorption peaks for Rb_3InCl_6 and Cs_3InCl_6, indicating limited visible-light absorption. In contrast, modest absorption peaks are observed for the bromide-based compounds, reaching 0.07 $\times$ 10^5 cm^{-1} for Rb_3InBr_6 and 0.0846 $\times$ 10^5 cm^{-1} for Cs_3InBr_6. The I-based compounds exhibit more pronounced visible-range absorption, with peak values of 0.0938 $\times$ 10^5 cm^{-1} for Rb_3InI_6 and 0.113 $\times$ 10^5 cm^{-1} for Cs_3InI_6, confirming their superior visible-light harvesting capability among all studied materials. In the UV region, strong absorption is observed for all compositions, as evident in Fig. 5(a). The maximum absorption coefficients reach 1.76 $\times$ 10^5 cm^{-1} at 16 eV for Rb_3InCl_6, 1.393 $\times$ 10^5 cm^{-1} at 7.64 eV for Rb_3InBr_6, and 1.449 $\times$ 10^5 cm^{-1} at 6.52 eV for Rb_3InI_6. For the Cs-based compounds, even higher maxima are obtained, with 3.035 $\times$ 10^5 cm^{-1} at 15.07 eV for Cs_3InCl_6, 2.698 $\times$ 10^5 cm^{-1} at 14.785 eV for Cs_3InBr_6, and 1.335 $\times$ 10^5 cm^{-1} at 6.257 eV for Cs_3InI_6. These strong UV responses originate from high-energy

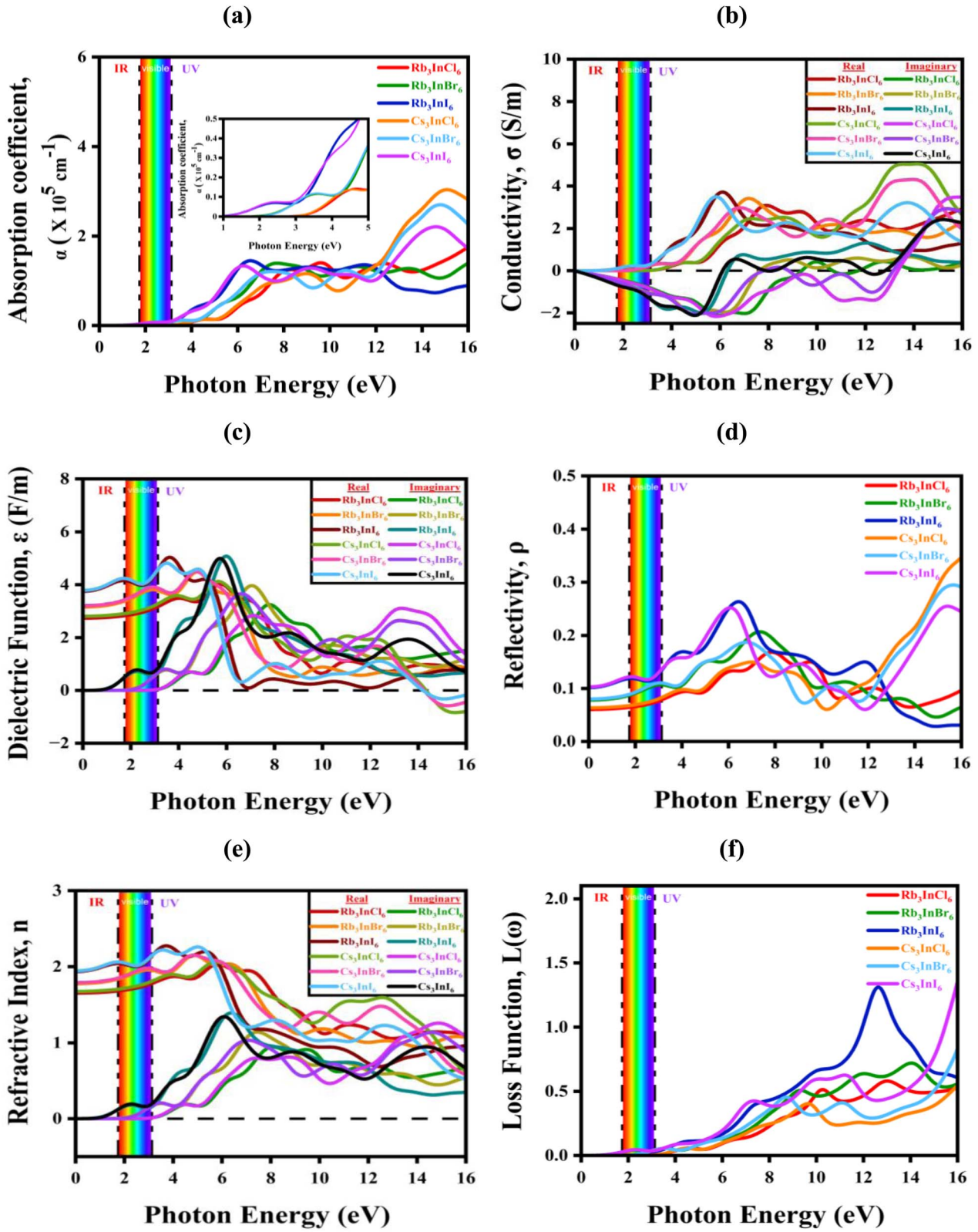

Fig. 5 Optical properties of (a) absorption coefficient, (b) conductivity, (c) dielectric function, (d) reflectivity, (e) refractive index, (f) loss function of A_3InX_6 defect-perovskite materials.

interband electronic transitions. Overall, the absorption behavior depicted in Fig. 5(a)-characterized by negligible IR absorption, enhanced visible-light absorption for I- and Br-based compounds, and strong UV absorption for all materials-demonstrates the suitability of A_3InX_6 compounds for solar cells, UV-visible photodetectors, and advanced optoelectronic devices.

3.4.2. Conductivity (σ). Optical conductivity describes the electronic response of a material under electromagnetic excitation and is derived from the complex dielectric function using standard relations.[66,67] The detailed expressions used in the calculations are provided in the SI eqn (S4). Fig. 5(b) presents the real part of the conductivity, it is observed that no noticeable response appears in the infrared (IR) region for the Cl- and Br-based compounds, whereas the I-based compounds exhibit finite conductivity contributions. In the visible region, the Cl-based compounds show no observable conductivity peaks, indicating weak optical activity.[68,69] In contrast, the Br-based materials begin to exhibit conductivity at photon energies of 2.44 eV and 2.57 eV for Rb_3InBr_6 and Cs_3InBr_6, respectively, where moderate conductivity values are observed throughout the visible range. Notably, the I-based compounds show pronounced visible-region peaks, with maximum values of 0.4098 at 3.10 eV for Rb_3InI_6 and 0.35 at 3.10 eV for Cs_3InI_6, demonstrating stronger optical conductivity compared to the Cl- and Br-based counterparts. With further increase in photon energy into the UV region, the real part of the conductivity increases significantly for all compounds, accompanied by multiple distinct peaks across the energy spectrum. The maximum UV-region conductivity peaks are observed at 3.08 at 7.91 eV for Rb_3InCl_6, 3.41 at 7.19 eV for Rb_3InBr_6, 3.71 at 6.106 eV for Rb_3InI_6, 5.04 at 13.857 eV for Cs_3InCl_6, 4.31 at 13.95 eV for Cs_3InBr_6, and 3.487 at 5.797 eV for Cs_3InI_6.

The imaginary part of the conductivity is also shown in Fig. 5(b). For all compounds, it initially exhibits negative values at low photon energies. This negative imaginary conductivity originates from a capacitive-like response of bound charge carriers, where the induced current lags behind the applied electromagnetic field due to polarization and carrier inertia effects. As the photon energy increases, the magnitude of the negative conductivity grows across the IR and visible regions and reaches maximum negative peaks in the UV region, with values of −2.165 at 5.905 eV, −2.079 at 5.00 eV, −1.862 at 5.312 eV, −2.1587 at 5.964 eV, −1.87 at 5.70 eV, and −2.103 at 5.045 eV for the A_3InX_6 compounds, respectively. With a further increase in photon energy, the imaginary part decreases in magnitude and crosses zero at 9.375 eV, 7.615 eV, 6.298 eV, 13.367 eV, 7.928 eV, and 6.11 eV, respectively. This zero-crossing behavior signifies a transition in the phase relationship between the induced current and the external field, typically associated with electronic resonance and interband transition thresholds. Beyond these energies, the imaginary part becomes positive, indicating an inductive-like response dominated by high-energy interband transitions, where the current leads the applied field and energy exchange is governed by rapid electronic oscillations.

3.4.3. Dielectric function. The optical dielectric response of the A_3InX_6 compounds is shown in Fig. 5(c). The optical behavior is described by the complex frequency-dependent dielectric function, whose real and imaginary components characterize the polarization and absorption responses of the material, respectively.[65–67] The detailed expressions used for calculating the dielectric function are provided in the SI eqn (S5)–(S7). The real part, $\varepsilon_1(\omega)$, represents the dispersive response of the material and is associated with electronic polarization and dielectric screening. It reflects how efficiently the material stores electromagnetic energy and influences key optical properties such as refractive index, phase velocity, and reflectivity. Positive values of $\varepsilon_1(\omega)$ indicate normal dielectric behavior, whereas a decrease or sign change signifies strong interband transitions and plasmon-related effects.

The real part of the dielectric function, $\varepsilon_1(\omega)$, for the A_3InX_6 defect-perovskite materials is presented in Fig. 5(c). At zero photon energy, $\varepsilon_1(\omega)$ starts with values of 2.729, 3.154, and 3.750 for Rb_3InCl_6, Rb_3InBr_6, and Rb_3InI_6, respectively, and 2.805, 3.203, and 3.787 for Cs_3InCl_6, Cs_3InBr_6, and Cs_3InI_6, reflecting the static dielectric constants of these compounds. As the photon energy increases across the IR and visible regions, the real part of the dielectric function gradually increases, indicating enhanced electronic polarization and dielectric screening. Several pronounced peaks are observed, corresponding to strong interband electronic transitions. The maximum values of ε_1 are 4.015 at 5.75 eV, 4.487 at 4.78 eV, and 5.038 at 3.634 eV for Rb_3InCl_6, Rb_3InBr_6, and Rb_3InI_6, respectively, while Cs_3InCl_6, Cs_3InBr_6, and Cs_3InI_6 reach maxima of 4.123 at 5.63 eV, 4.496 at 4.74 eV, and 4.814 at 3.499 eV, respectively. With further increase in photon energy into the UV region, $\varepsilon_1(\omega)$ decreases due to reduced polarization response at higher excitation energies. Notably, the Cs-based compounds exhibit zero-crossing behavior at 14.347 eV (Cs_3InCl_6), 14.239 eV (Cs_3InBr_6), and 14.197 eV (Cs_3InI_6), beyond which $\varepsilon_1(\omega)$ becomes negative, indicating plasma-like behavior and strong reflectivity in the high-energy region.

The imaginary part $\varepsilon_2(\omega)$, which represents optical absorption due to interband electronic transitions. The onset of $\varepsilon_2(\omega)$ occurs at photon energies of 3.515 eV, 2.440 eV, and 1.335 eV for Rb_3InCl_6, Rb_3InBr_6, and Rb_3InI_6, respectively, while the corresponding thresholds for the Cs-based compounds are 3.567 eV (Cs_3InCl_6), 2.570 eV (Cs_3InBr_6), and 1.430 eV (Cs_3InI_6). These onset energies are closely associated with the fundamental band gaps of the respective materials.

As the photon energy increases, $\varepsilon_2(\omega)$ increases steadily, indicating enhanced optical absorption due to stronger interband transitions, and reaches pronounced maxima in the UV region. The peak values for the Rb-based compounds are 3.23 at 7.76 eV, 3.96 at 7.04 eV, and 5.06 at 5.91 eV for Rb_3InCl_6, Rb_3InBr_6, and Rb_3InI_6, respectively. Similarly, the Cs-based compounds exhibit maximum $\varepsilon_2(\omega)$ values of 3.09 at 13.41 eV for Cs_3InCl_6, 3.65 at 6.547 eV for Cs_3InBr_6, and 4.99 at 5.69 eV for Cs_3InI_6. The stronger and lower-energy peaks observed for the I-based compounds further confirm their enhanced optical absorption and higher electronic polarizability compared to the Cl- and Br-based systems.

3.4.4. Reflectivity. Reflectivity describes the fraction of incident electromagnetic radiation reflected from the material surface and was calculated from the complex dielectric function using standard relations.[71] The detailed expressions used in the calculations are provided in the SI in eqn (S8).[72]

The presented spectra in Fig. 5(d), the reflectivity values begin around 0.07 to 0.11 at low photon energies (near 0 eV), indicating relatively weak reflection in the infrared region. The highest reflectivity peak is observed for Cs_3InCl_6, reaching above 0.35 at about 15 eV, showing strong reflection in the deep

UV region. Cs_3InI_6 also exhibits a significant peak close to 0.27 around 7 eV, while Cs_3InBr_6 and Rb_3InI_6 display intermediate peaks between 0.2 to 0.25 around 6 to 8 eV. In contrast, Rb_3InCl_6 shows the lowest overall reflectivity, with peaks not exceeding 0.18. The closest comparable values appear for Rb_3InBr_6 and Rb_3InI_6 in the visible-UV transition region (3 to 7 eV), suggesting similar photon–electron interaction strengths. These trends imply that Cs-based halide perovskites generally exhibit stronger reflectivity responses than their Rb analogues, especially in the higher-energy UV range. From an application perspective, the high reflectivity of Cs_3InCl_6 at deep UV energies suggests potential as a UV-protective or reflective coating material, while Cs_3InI_6, with its pronounced peak around 7 eV, may serve in UV-visible optoelectronics and detectors. Rb_3InX_6 compounds, with comparatively lower reflectivity across the spectrum, could be more favorable in solar energy harvesting applications where reduced reflection (hence greater absorption) is desired to maximize photon capture. The systematic variation of peaks across halides also demonstrates tunability, making these materials candidates for wavelength-selective mirrors, filters, or optoelectronic interfaces.[73–75] Thus, calculating reflectivity is crucial to evaluate and optimize the suitability of A_3InX_6 perovskites for photovoltaic devices, photodetectors, and coating technologies.

3.4.5. Refractive index. The refractive index were calculated from the complex dielectric function using standard optical relations shown in SI eqn (S9)–(S11).[70–72] The variation of the $\eta(\omega)$ for the A_3InX_6 defect-perovskite compounds is presented in Fig. 5(e). At zero photon energy, the $\eta(\omega)$ starts at 1.675, 1.790, and 1.947 for Rb_3InCl_6, Rb_3InBr_6, and Rb_3InI_6, respectively, while identical initial values of 1.675, 1.790, and 1.948 are obtained for the corresponding Cs_3InCl_6, Cs_3InBr_6, and Cs_3InI_6 compounds. These values reflect the static refractive indices and increase systematically from Cl to I due to enhanced electronic polarizability. With increasing photon energy, $\eta(\omega)$ increases in the IR and visible regions, reaching maximum values of 2.056 at 6.0 eV for Rb_3InCl_6, 2.150 at 4.89 eV for Rb_3InBr_6, and 2.276 at 3.73 eV for Rb_3InI_6. Beyond these energies, further increase in photon energy leads to a gradual decrease in the refractive index up to 16 eV, indicating reduced optical dispersion at higher energies. A similar trend is observed for the Cs-based compounds, where $\eta(\omega)$ increases with photon energy and attains maximum values of 2.070 at 5.87 eV for Cs_3InCl_6, 2.150 at 4.89 eV for Cs_3InBr_6, and 2.260 at 4.983 eV for Cs_3InI_6. At higher photon energies, the refractive index decreases; however, for the Cs-based materials, $\eta(\omega)$ remains relatively elevated up to approximately 14 eV before showing a more pronounced decline. Overall, the refractive index follows the trend I > Br > Cl, consistent with the dielectric response and optical conductivity results.

As shown in Fig. 5(e), the imaginary part of the refractive index remains nearly zero in the IR region for all A_3InX_6 compounds, indicating negligible absorption at low photon energies. In the visible region, the Cl-based compounds exhibit very weak $k(\omega)$ values, confirming their low absorption and wide band-gap nature. In contrast, the Br-based materials show a gradual increase in $k(\omega)$, while the I-based compounds display a more pronounced rise, reflecting their enhanced optical absorption due to narrower band gaps. With further increase in photon energy into the UV region, the imaginary part of the refractive index increases significantly for all materials and exhibits multiple distinct peaks. These peaks originate from strong interband transitions involving deeper valence-band states. Among all compounds, the I-based materials show the highest $k(\omega)$ values, indicating stronger absorption losses, followed by the Br-based and Cl-based systems. Additionally, the Cs-based compounds generally exhibit slightly higher and broader absorption features than their Rb-based counterparts, suggesting enhanced optical transition strength at higher photon energies. Overall, the variation of the imaginary part of the refractive index confirms that halide substitution plays a dominant role in controlling optical absorption in A_3InX_6 defect-perovskites, with iodine-based compounds being the most optically active across the visible and UV spectral regions.

3.4.6. Loss function. The energy loss function, $L(\omega)$, derived from the complex dielectric function, describes the energy dissipation of fast electrons interacting with the material and is commonly used to identify plasmon resonances.[76] From the plotted spectra in Fig. 5(f), the highest peak is observed for Rb_3InI_6 around ~12.5 eV, followed closely by Cs_3InI_6 near ~13.5 eV, indicating strong plasmonic resonance and enhanced electron–photon interactions. The lowest peak response is found for Cs_3InCl_6 (~9.5 to 10 eV), reflecting weaker plasmon activity due to its wider band gap and lower polarizability. The intermediate responses are seen for Rb_3InCl_6 and Rb_3InBr_6 (~10 to 12 eV), and Cs_3InBr_6 (~11 to 12 eV), suggesting moderate plasmonic activity. Based on these peak values, Rb_3InI_6 and Cs_3InI_6 are promising for ultraviolet (UV) plasmonic devices, high-frequency optoelectronics, and radiation detectors; Br-based compounds (Rb_3InBr_6, Cs_3InBr_6) may be suitable for visible to near-UV applications such as light-harvesting and LEDs, while Cl-based perovskites (Rb_3InCl_6, Cs_3InCl_6) are better suited for high-energy UV filters and insulating optical coatings due to their higher stability and weaker loss response. Thus, the loss function analysis highlights how halogen substitution modulates the plasmonic and dielectric properties of these compounds, guiding their application in solar cells, sensors, and high-frequency photonic technologies.

3.5. Elastic and mechanical properties

3.5.1. Elastic properties. The elastic constants provide essential information on the mechanical response, stiffness, and stability of crystalline materials under external stress. Within the linear elastic regime, the stress–strain relationship is governed by Hooke's law,[77]

$$\sigma_i = \sum C_{ij}\varepsilon_j \quad (3)$$

where C_{ij} are the elastic stiffness coefficients. For a cubic crystal system, only three independent elastic constants exist, namely C_{11}, C_{12}, and C_{44}. Here, C_{11} describes resistance to uniaxial deformation, C_{12} represents the elastic coupling between longitudinal and transverse strains, and C_{44} corresponds to resistance against shear deformation.

Fig. 6 illustrates the calculated elastic constants of the A_3InX_6 defect-perovskites. For each investigated compound, the elastic constants follow the relation,

$$C_{11} > C_{12} > C_{44}$$

indicating that the resistance to longitudinal (axial) deformation is greater than that to shear deformation. This ordering is characteristic of many crystalline solids and reflects the intrinsic mechanical response of the lattice under different modes of strain. It should be noted that this relation describes the relative magnitude of elastic constants within a given compound and is independent of compositional trends.

When comparing different halide compositions, the variation of the elastic constants does not follow a strictly monotonic trend. In the Rb-based series, C_{11} decreases from Rb_3InCl_6 (32.538 GPa) to Rb_3InBr_6 (26.553 GPa) and further to Rb_3InI_6 (16.779 GPa), suggesting a progressive reduction in lattice stiffness with increasing halide ionic radius. A similar decrease is observed for C_{12} and C_{44} within this series. In contrast, the Cs-based compounds exhibit non-monotonic behavior. Specifically, C_{11} increases from Cs_3InCl_6 (31.50 GPa) to Cs_3InBr_6 (40.186 GPa), followed by a significant decrease for Cs_3InI_6 (16.677 GPa). This indicates that substitution of Cl by Br enhances lattice stiffness, possibly due to improved orbital interactions or bonding characteristics, whereas further substitution with the larger I^- ion leads to lattice softening due to increased bond length and reduced bond strength. Similar non-monotonic variations are also observed in C_{12} and C_{44}. These results demonstrate that elastic properties in these systems are governed by a balance between ionic size, bond strength, and structural distortion, and therefore cannot be described by a single systematic trend across all compositions.

The mechanical stability of the cubic A_3InX_6 compounds is evaluated using the Born stability criteria, which for cubic symmetry are given by:[78,79]

$$C_{11} - C_{12} > 0,\ C_{11} + 2C_{12} > 0 \text{ and } C_{11} > 0,\ C_{44} > 0 \quad (4)$$

All calculated elastic constants satisfy these conditions, confirming that the investigated compounds are mechanically stable at ambient pressure. Overall, the moderate elastic stiffness and tunable mechanical properties achieved through halide substitution indicate that A_3InX_6 defect-perovskites possess adequate structural stability for optoelectronic and energy-related applications.

3.5.2. Mechanical properties. The mechanical properties of crystalline materials describe their ability to withstand external forces without failure and are essential for evaluating structural integrity, durability, and practical applicability. These properties govern how a material responds to compression, tension, and shear, and they play a critical role in determining mechanical reliability in device-level and engineering applications.[80]

The bulk modulus (B) quantifies the resistance of a material to uniform volume compression and serves as a direct measure of incompressibility. Materials with higher bulk modulus values exhibit stronger interatomic bonding and greater resistance to externally applied pressure. Conventionally, materials with B > 40 GPa are considered mechanically hard, whereas those with B < 40 GPa are classified as relatively flexible or soft. In the present work, the bulk modulus is evaluated using the Voigt–Reuss–Hill (VRH) approximation, where the Hill average provides a reliable estimate of the polycrystalline bulk modulus:[81]

$$B = \frac{B_V + B_R}{2} \quad (5)$$

with the Voigt and Reuss bounds for cubic symmetry given by:

$$B_V = B_R = \frac{C_{11} + 2C_{12}}{3} \quad (6)$$

The calculated bulk modulus values are presented in Fig. 7(a). The Rb-based compounds exhibit bulk moduli of 14.027 GPa (Rb_3InCl_6), 11.79 GPa (Rb_3InBr_6), and 8.672 GPa (Rb_3InI_6), showing a systematic decrease from Cl to I, which reflects the weakening of interatomic interactions with increasing halide ionic radius. Similarly, the Cs-based materials

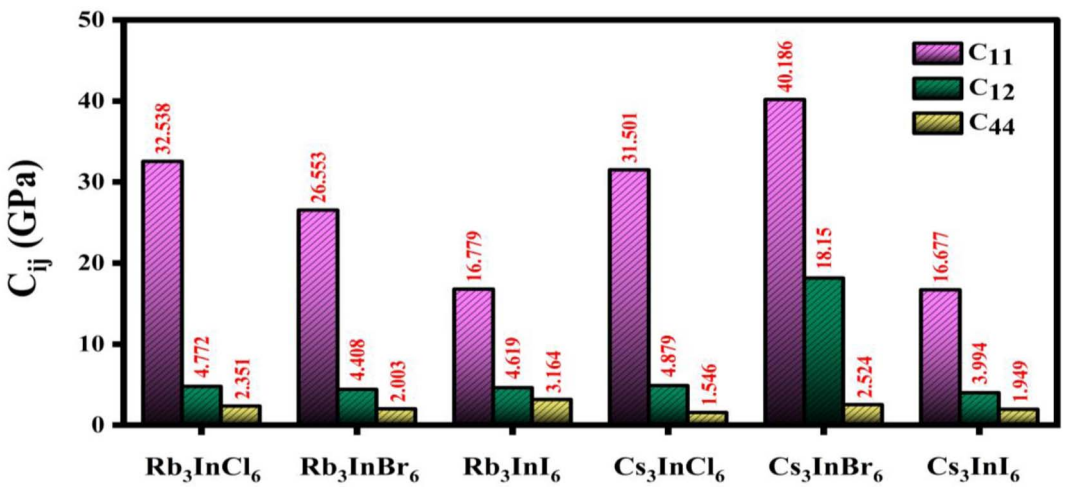

Fig. 6 Elastic constant of A_3InX_6 defect perovskite materials.

show bulk moduli of 13.753 GPa (Cs_3InCl_6), 25.495 GPa (Cs_3InBr_6), and 8.221 GPa (Cs_3InI_6). Among all compounds, Cs_3InBr_6 exhibits the highest bulk modulus, indicating comparatively stronger resistance to compression. Overall, all investigated A_3InX_6 compounds possess bulk modulus values well below 40 GPa, confirming their mechanically soft and flexible nature, which is advantageous for applications requiring strain tolerance and mechanical adaptability, such as flexible optoelectronic and energy-conversion devices.

The shear modulus (G) describes a material's resistance to shape change under applied shear stress and is an important indicator of rigidity against transverse deformation. A higher shear modulus signifies stronger resistance to distortion and improved mechanical rigidity. The shear modulus is given by:[82]

$$G_V = \frac{C_{11} - C_{12} + 3C_{44}}{5} \quad (7)$$

$$G_R = \frac{5C_{44}(C_{11} - C_{12})}{[4C_{44} + 3(C_{11} - C_{12})]} \quad (8)$$

$$G = \frac{G_V + B_R}{2} \quad (9)$$

The calculated shear modulus values are presented in Fig. 7(b). The Rb-based compounds exhibit shear moduli of 5.242 GPa (Rb_3InCl_6), 4.305 GPa (Rb_3InBr_6), and 4.123 GPa (Rb_3InI_6), indicating a gradual reduction in rigidity with halide substitution from Cl to I. Similarly, the Cs-based materials show shear modulus values of 4.322 GPa (Cs_3InCl_6), 4.785 GPa (Cs_3InBr_6), and 3.201 GPa (Cs_3InI_6). Among all compounds, Rb_3InCl_6 and Cs_3InBr_6 exhibit comparatively higher shear resistance, while the I-based materials display lower values, confirming their mechanically softer nature.

The Young's modulus (Y) characterizes the tensile stiffness of a material and defines the extent of elastic deformation under uniaxial tensile or compressive loading. A higher value of Y indicates greater stiffness and stronger resistance to elongation, whereas lower values correspond to mechanically softer and more flexible materials.[83]

$$Y = \frac{9BG}{(3B + G)} \quad (10)$$

The calculated Y values are displayed in Fig. 7(c). The Rb-based compounds exhibit Y of 13.985 GPa (Rb_3InCl_6), 11.515 GPa (Rb_3InBr_6), and 10.677 GPa (Rb_3InI_6), showing a decreasing trend from Cl to I due to progressive weakening of interatomic bonding. Similarly, the Cs-based materials show Young's moduli of 11.737 GPa (Cs_3InCl_6), 13.511 GPa (Cs_3InBr_6), and 8.501 GPa (Cs_3InI_6). Among all compounds, Rb_3InCl_6 and Cs_3InBr_6 exhibit the highest tensile stiffness, while Cs_3InI_6 shows the lowest Young's modulus, indicating enhanced mechanical flexibility.

The ductile or brittle nature of the A_3InX_6 defect-perovskite compounds is assessed using both Poisson's ratio (ν) and Pugh's ratio (B/G), as shown in Fig. 7(d) and (e). According to established criteria, materials with $\nu > 0.26$ and $B/G > 1.75$ are classified as ductile, whereas lower values indicate brittle behavior.[84]

$$\nu = \frac{3B - 2G}{2(3B + G)} \quad (11)$$

As presented in Fig. 7(d), Poisson's ratio values for the Rb-based compounds are 0.333 (Rb_3InCl_6), 0.337 (Rb_3InBr_6), and 0.294 (Rb_3InI_6), while the Cs-based materials exhibit values of 0.357 (Cs_3InCl_6), 0.411 (Cs_3InBr_6), and 0.327 (Cs_3InI_6). All values exceed the critical limit of 0.26, indicating a clear ductile mechanical response.

Consistently, the Pugh's ratio values shown in Fig. 7(e) further confirm the ductile nature of these materials. The Rb-based compounds exhibit B/G ratios of 2.676, 2.739, and 2.103 for Rb_3InCl_6, Rb_3InBr_6, and Rb_3InI_6, respectively, while the Cs-based compounds show significantly higher values of 3.182 (Cs_3InCl_6), 5.328 (Cs_3InBr_6), and 2.568 (Cs_3InI_6). All values are well above the ductility threshold of 1.75. Overall, the combined analysis of Poisson's ratio and Pugh's ratio demonstrates that all A_3InX_6 compounds are mechanically ductile, with Cs-based systems-particularly Cs_3InBr_6-showing superior plastic deformability. This intrinsic ductility enhances mechanical reliability and supports the suitability of these materials for flexible and strain-tolerant optoelectronic and energy-related applications.

Hardness is an important mechanical parameter that reflects a material's resistance to permanent (plastic) deformation, scratching, and wear. The Vickers hardness (H_V) is estimated using Tian's empirical model. It is expressed as:[85]

$$H_V = \frac{(1 - 2\nu)}{6(1 + \nu)} \quad (12)$$

The calculated hardness values are presented in Fig. 7(f). The Rb-based compounds exhibit hardness values of 1.639 GPa (Rb_3InCl_6), 1.380 GPa (Rb_3InBr_6), and 1.179 GPa (Rb_3InI_6), showing a systematic decrease from Cl to I. This trend is attributed to the progressive weakening of interatomic bonding and increased lattice softness with heavier halide substitution. Similarly, the Cs-based compounds show hardness values of 1.374 GPa (Cs_3InCl_6), 0.636 GPa (Cs_3InBr_6), and 0.940 GPa (Cs_3InI_6). Among all materials, Rb_3InCl_6 exhibits the highest hardness, while Cs_3InBr_6 shows the lowest value, indicating enhanced mechanical softness.

The machinability index (μ_M) is an important mechanical parameter that evaluates the ease with which a material can be machined, cut, or shaped without inducing excessive damage. It is defined as,[86]

$$\mu_M = \frac{B}{C_{44}} \quad (13)$$

A higher machinability index indicates better machinability, implying lower resistance to shear deformation and improved workability. The calculated machinability indices are presented

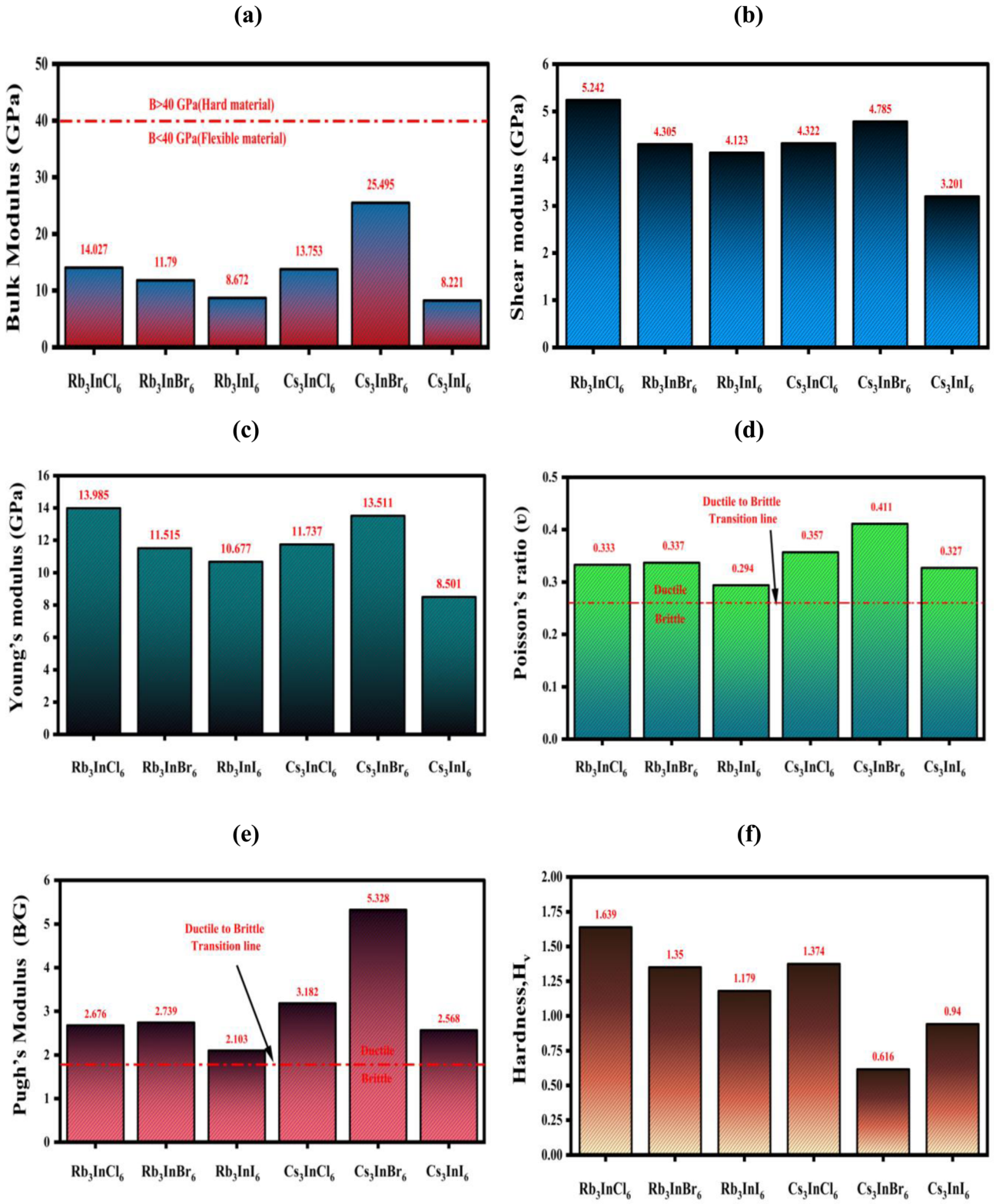

Fig. 7 Mechanical properties in the (a) bulk modulus, (b) shear modulus, (c) Young's modulus, (d) Poisson ratio, (e) Pugh's ratio, and (f) hardness of the A_3InX_6 defect-perovskite materials.

in Fig. 8(a). The Rb-based compounds exhibit μ_M values of 5.968 (Rb_3InCl_6), 5.885 (Rb_3InBr_6), and 2.740 (Rb_3InI_6), showing a notable reduction for the I-based compound, which reflects increased resistance to shear deformation. In contrast, the Cs-based materials display higher machinability indices of 8.896 (Cs_3InCl_6), 10.100 (Cs_3InBr_6), and 4.218 (Cs_3InI_6). Among all investigated compounds, Cs_3InBr_6 exhibits the highest

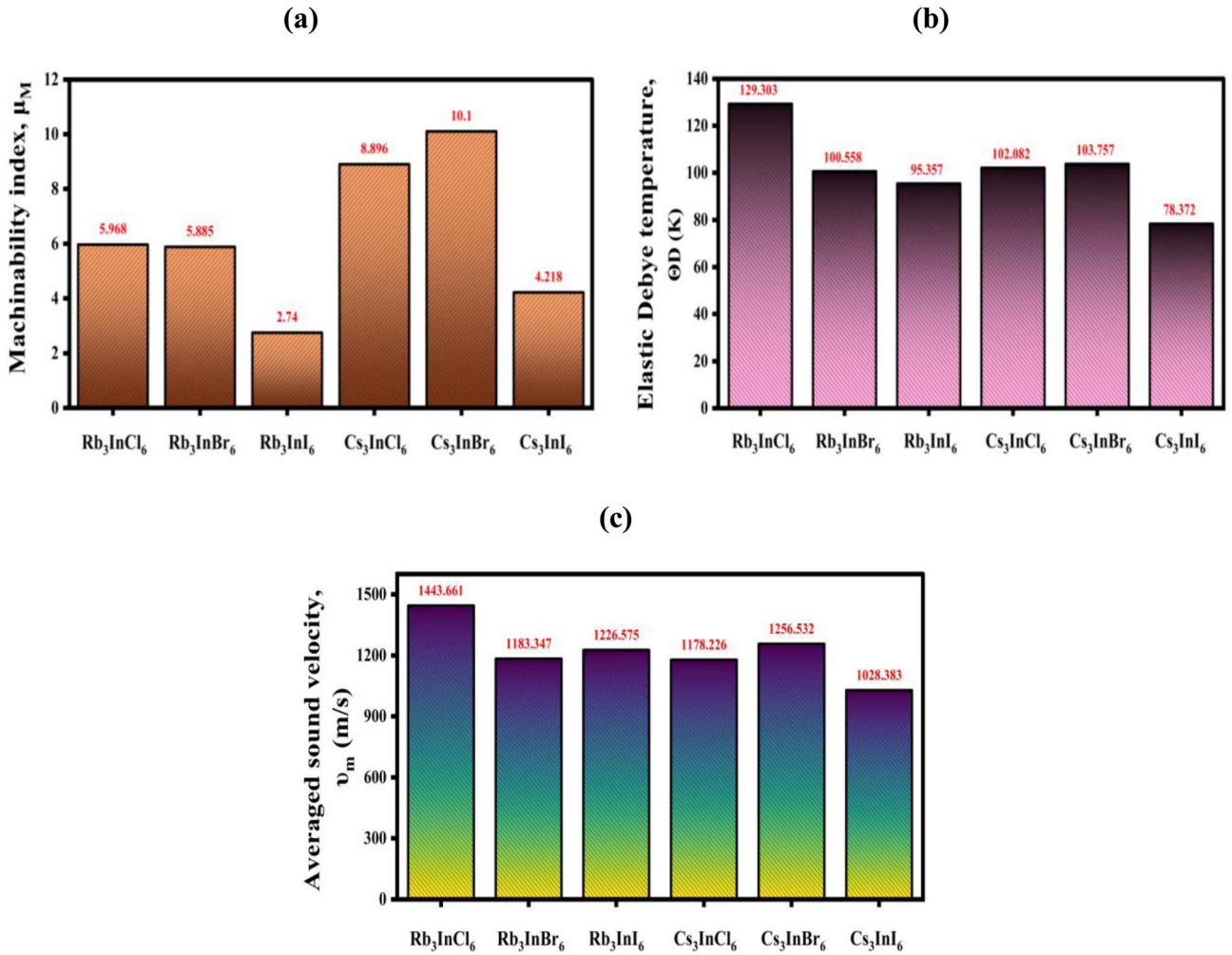

Fig. 8 Mechanical parameters of (a) machinability index, (b) elastic Debye temperature, (c) average sound velocity of A_3InX_6 defect perovskite materials.

machinability index, indicating superior machinability and ease of fabrication.

The Debye temperature (Θ_D) is an important thermophysical parameter that provides insight into lattice vibrations, bonding strength, and thermal behavior of crystalline materials. It is closely related to the average sound velocity and elastic properties, and higher Debye temperatures generally indicate stronger interatomic bonding, higher phonon frequencies, and improved lattice rigidity. In this work, the elastic Debye temperature is evaluated from the elastic moduli through the average sound velocity, reflecting the vibrational contribution of the crystal lattice. The calculated Debye temperatures are presented in Fig. 8(b). The Rb-based compounds exhibit Debye temperatures of 129.303 K (Rb_3InCl_6), 100.558 K (Rb_3InBr_6), and 95.357 K (Rb_3InI_6), showing a clear decreasing trend from Cl to I. This reduction is attributed to the increasing atomic mass of the halide ions and the corresponding softening of lattice vibrations. Similarly, the Cs-based compounds show Debye temperatures of 102.082 K (Cs_3InCl_6), 103.757 K (Cs_3InBr_6), and 78.372 K (Cs_3InI_6). Among all investigated materials, Rb_3InCl_6 exhibits the highest Debye temperature, indicating comparatively stronger bonding and higher lattice vibrational frequencies, whereas Cs_3InI_6 shows the lowest value, reflecting enhanced lattice softness and weaker bonding interactions.

The average sound velocity (V_m) is a key elastic parameter that reflects the propagation of acoustic phonons in a crystal lattice and is directly related to the elastic moduli and atomic density of the material. It plays an important role in determining thermophysical properties such as the Debye temperature and lattice thermal conductivity. Generally, higher sound velocity indicates stronger interatomic bonding and greater lattice stiffness. The calculated V_m for the A_3InX_6 defect-perovskites are presented in Fig. 8(b). The Rb-based compounds exhibit sound velocities of 1443.661 m s^{-1} (Rb_3InCl_6), 1183.347 m s^{-1} (Rb_3InBr_6), and 1226.575 m s^{-1} (Rb_3InI_6). Among these, Rb_3InCl_6 shows the highest sound velocity, consistent with its higher elastic stiffness and Debye temperature. For the Cs-based compounds, the average sound velocities are 1178.226 m s^{-1} (Cs_3InCl_6), 1256.532 m s^{-1} (Cs_3InBr_6), and 1028.383 m s^{-1} (Cs_3InI_6). The lower V_m observed for Cs_3InI_6 reflects its softer lattice and weaker bonding interactions. Overall, a general decrease in V_m is observed with halide

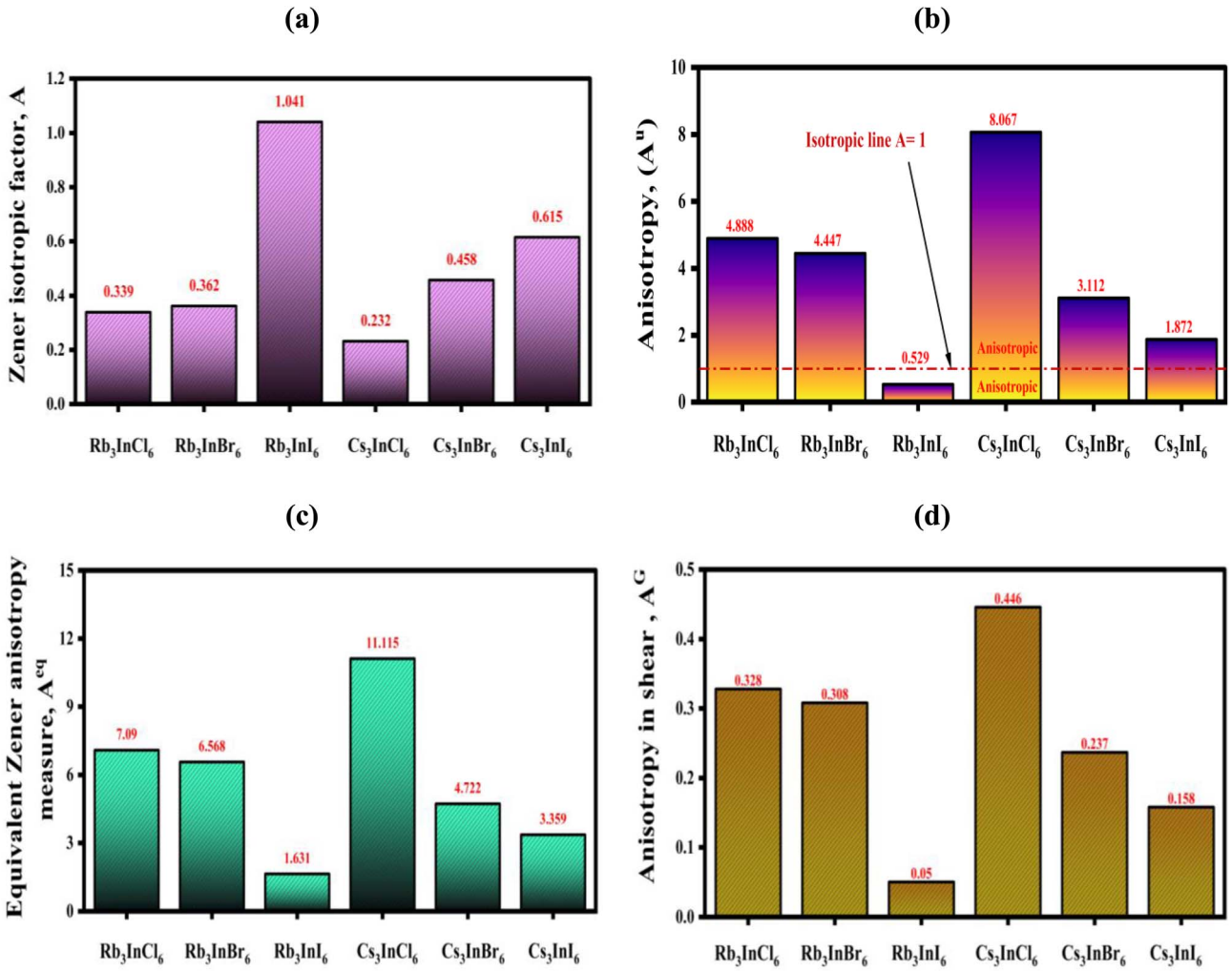

Fig. 9 Mechanical parameters of (a) Zener isotropic factor (A), (b) anisotropy (A^{U}), (c) equivalent Zener anisotropy measure (A^{eq}), and (d) anisotropy in shear (A^{G}) of the A_3InX_6 defect perovskite materials.

substitution from Cl to I, which is attributed to the increased atomic mass and reduced force constants.

These results are in good agreement with the calculated Debye temperatures, confirming that the vibrational and elastic properties of A_3InX_6 defect-perovskites are strongly influenced by halide composition. The relatively low sound velocities indicate soft lattice dynamics, which may be beneficial for applications requiring mechanical flexibility and could also impact thermal transport behavior in energy and optoelectronic devices.

3.5.3. Anisotropy properties. Elastic anisotropy reflects the directional dependence of mechanical properties and plays a critical role in understanding deformation behavior, crack propagation, and mechanical reliability of crystalline materials. To achieve a comprehensive evaluation of anisotropic behavior, both the Zener anisotropy factor (A) and the universal elastic anisotropy index (A^{U}) are employed, as they provide complementary measures of elastic anisotropy. The Zener anisotropy factor, defined for cubic symmetry as[87]

$$A = \frac{2C_{44}}{C_{11} - C_{12}} \quad (14)$$

quantifies shear anisotropy. For an elastically isotropic material, $A = 1$, whereas deviations from unity indicate anisotropic mechanical behavior.[87] As shown in Fig. 9(a), the Rb-based compounds exhibit Zener factors of 0.339 (Rb_3InCl_6), 0.362 (Rb_3InBr_6), and 1.041 (Rb_3InI_6), indicating pronounced anisotropy for the Cl- and Br-based compounds and nearly isotropic behavior for Rb_3InI_6. Similarly, the Cs-based materials show values of 0.232 (Cs_3InCl_6), 0.458 (Cs_3InBr_6), and 0.615 (Cs_3InI_6), confirming anisotropic elastic behavior across the Cs series, with reduced anisotropy for the I-based compound. The universal elastic anisotropy index (A^{U}), defined as

$$A^{U} = \frac{B_V}{B_r} + 5\frac{G_V}{B_R} - 6 \geq 0 \quad (15)$$

provides a global measure of elastic anisotropy, where $A^{U} = 0$ corresponds to perfect isotropy and increasing values indicate stronger directional dependence. The calculated anisotropy indices are shown in Fig. 9(b). The Rb-based compounds exhibit

A^U values of 4.888 (Rb_3InCl_6), 4.447 (Rb_3InBr_6), and 0.529 (Rb_3InI_6), indicating moderate to low elastic anisotropy, with Rb_3InI_6 approaching near-isotropic behavior. In contrast, the Cs-based materials show values of 8.067 (Cs_3InCl_6), 3.112 (Cs_3InBr_6), and 1.872 (Cs_3InI_6), revealing generally higher anisotropy, particularly for Cs_3InCl_6, which exhibits the most pronounced directional dependence among all compounds. Overall, both the Zener anisotropy factor and the universal elastic anisotropy index consistently demonstrate that elastic anisotropy decreases with halide substitution from Cl to I in the A_3InX_6 defect-perovskites. The near-isotropic elastic response observed for Rb_3InI_6, along with reduced anisotropy in other I-based compounds, is advantageous for minimizing stress concentration and enhancing mechanical reliability, which are essential for optoelectronic and energy-related applications.

To further quantify elastic anisotropy in a unified and comparable manner, the equivalent Zener anisotropic measure (A^{eq}) is employed. This parameter transforms the universal elastic anisotropy index into an equivalent Zener-type measure, allowing direct comparison of anisotropy strength on a common scale. It is defined as:[88]

$$A^{eq} = \left(1 + \frac{5}{12}A^U\right) + \sqrt{\left(1 + \frac{5}{12}A^U\right)^2 - 1} \quad (16)$$

The calculated A^{eq} values are presented in Fig. 9(c). The Rb-based compounds exhibit equivalent Zener measures of 7.09 (Rb_3InCl_6), 6.568 (Rb_3InBr_6), and 1.631 (Rb_3InI_6), indicating strong anisotropy for the Cl- and Br-based compounds and significantly reduced anisotropy for Rb_3InI_6, which approaches near-isotropic behavior. In contrast, the Cs-based materials show A^{eq} values of 11.115 (Cs_3InCl_6), 4.722 (Cs_3InBr_6), and 3.359 (Cs_3InI_6). Among all investigated compounds, Cs_3InCl_6 exhibits the highest A^{eq} value, confirming the strongest elastic anisotropy and pronounced directional dependence of mechanical property.

Elastic anisotropy in shear deformation is quantified using the shear anisotropy index (A^G), which evaluates the directional dependence of shear response in polycrystalline materials. It is defined as:[89]

$$A^G = \frac{G_V - G_R}{G_V + G_R} \quad (17)$$

A value of $A^G = 0$ corresponds to isotropic shear behavior, while increasing values indicate stronger anisotropy in shear response. The calculated shear anisotropy indices are presented in Fig. 9(d). The Rb-based compounds exhibit A^G values of 0.328 (Rb_3InCl_6), 0.308 (Rb_3InBr_6), and 0.050 (Rb_3InI_6), indicating moderate shear anisotropy for the Cl- and Br-based materials and nearly isotropic shear behavior for Rb_3InI_6. In contrast, the Cs-based compounds show A^G values of 0.446 (Cs_3InCl_6), 0.237 (Cs_3InBr_6), and 0.158 (Cs_3InI_6), revealing comparatively stronger shear anisotropy, particularly for Cs_3InCl_6, which exhibits the highest directional dependence in shear deformation. Overall, the A^{eq} and A^G follows the same halide-dependent trend observed in other anisotropy measures, decreasing from Cl to I substitution. The low A^{eq} and A^G values of the I-based compounds-especially Rb_3InI_6-indicate nearly uniform shear resistance along different crystallographic directions, which is beneficial for reducing stress concentration and improving mechanical reliability in device applications.

Anisotropy refers to the directional dependence of physical properties of a material, meaning that its mechanical, electronic, or optical responses vary when measured along different crystallographic directions.[90] In perovskites such as A_3InX_6 defect perovskite materials, anisotropy is particularly important because it provides insight into the stability, mechanical flexibility, and suitability of these compounds for optoelectronic applications. The elate tensor analysis was investigated with the aid of Google Colab using Python 3.0.[91] Fig. S1–S3 show 2D and 3D representations of Young's modulus, shear modulus, and Poisson's ratio, clearly reflecting the degree of anisotropy.

Fig. S1 compares two Rb-based compounds with different halides. In both, the Young's-modulus maps show the classic four-lobed, cross-shaped anisotropy, but the chloride has longer, sharper lobes and a larger 3D surface; it is stiffer and more anisotropic than the bromide. The shear-modulus plots are nearly perfect circles with gently oblate 3D shells for both materials, indicating an almost orientation-independent resistance to shear and only minor differences between Cl and Br. The Poisson's-ratio maps form four-petal flowers; the bromide exhibits slightly broader petals (greater directional variation), while the chloride is more uniform. Overall, replacing Cl by Br in the Rb compound softens the lattice and slightly increases ν anisotropy while leaving shear behavior essentially isotropic, useful guidance when balancing stiffness against compliance in Rb-based devices.

Fig. S2 places the softest and the stiffest ends of the series side-by-side. Rb_3InI_6 has the smallest, roundest Young's-modulus surface, signaling a compliant, weakly anisotropic lattice, whereas Cs_3InCl_6 shows the largest and most faceted E-surface, marking it as the stiffest member. Shear-modulus plots for both remain close to isotropic, with only subtle differences in shape and magnitude. In the Poisson's-ratio maps, Rb_3InI_6 presents wider petals (larger directional ν), indicating greater lateral strain for a given axial load; Cs_3InCl_6 is comparatively restrained. The juxtaposition demonstrates how composition can strongly tune mechanical response: moving from Rb–I to Cs–Cl dramatically increases stiffness while maintaining nearly uniform shear behavior critical for choosing between strain-accommodating layers (iodide) and mechanically robust layers (chloride).

In Fig. S3, the A-site cation is fixed (Cs) and only the halide changes. Young's-modulus maps show Cs_3InBr_6 with a larger, sharper four-lobed pattern than Cs_3InI_6, so the bromide is stiffer and more anisotropic, while the iodide is softer and more rounded. The shear-modulus plots again appear as near-circles with slightly oblate 3D shapes for both compounds, confirming that shear resistance is mostly orientation-independent and only marginally affected by the halide. Poisson's-ratio maps reveal stronger angular variation for the iodide (broader petals) than for the bromide, but ν remains positive throughout,

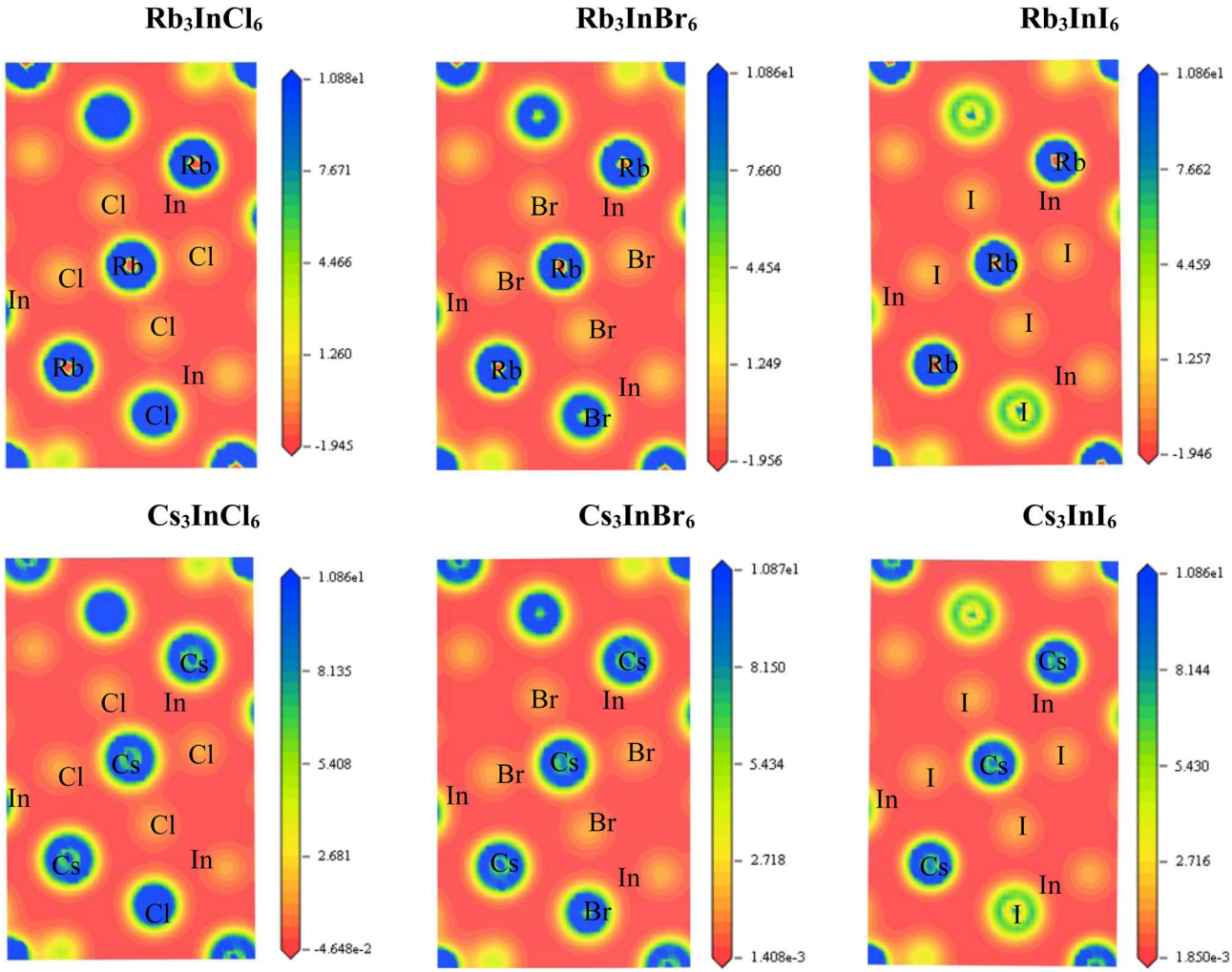

Fig. 10 Charge density mapping of A_3InX_6 (A = Rb, Cs, and X = Cl, Br, I) perovskite.

consistent with elastic stability. Collectively, this figure isolates the halide effect in Cs-based materials: Br → I decrease stiffness and increases ν anisotropy, a practical lever for tuning crack resistance and stress accommodation in Cs-containing perovskite layers. Collectively, the figures demonstrate that these perovskites are elastically stable, with shear behavior that is nearly orientation-independent, and that their axial stiffness and lateral-strain coupling can be tuned primarily through the halide harder, more anisotropic for Cl; softer, more compliant for I. This is mechanically significant for crystal growth and device engineering because it identifies orientations least likely to crack, guides texture control in thin films, and clarifies how composition can be used to balance robustness (chlorides) against compliance and stress accommodation (iodides).

3.6. Charge density

Fig. 10 illustrates the charge density mapping of A_3InX_6 (A = Rb, Cs; X = Cl, Br, I) halide double perovskites, highlighting the electronic distribution and bonding features.[67] The Rb-based compounds are presented in the top panels, while the Cs-based analogues are shown in the bottom panels. The color scale represents electron density, where red indicates regions of high electron concentration and blue corresponds to low electron density, with values ranging approximately from −1.95 to 10.86 e $Å^{-3}$. A pronounced charge localization is observed around the In and halogen (Cl, Br, I) atoms, with maximum density values approaching ~10.8 e $Å^{-3}$, reflecting their dominant role in bonding interactions. In contrast, the Rb and Cs atoms exhibit significantly lower electron density, indicating their largely ionic character and weaker participation in covalent bonding.

A systematic variation is observed across the halogen series: as X changes from Cl → Br → I, the electron density distribution becomes more spatially extended, indicating increased charge delocalization and a gradual shift in bonding character. Similarly, substitution of Rb with the larger Cs cation leads to a broader distribution of charge around the A-site, suggesting modifications in the local electrostatic environment and possible changes in orbital interactions with neighboring halogen atoms. These observations provide qualitative insight into the bonding nature and orbital hybridization within the A_3InX_6 lattice.

However, it should be noted that charge density analysis primarily reflects electronic distribution and bonding characteristics, and does not directly determine carrier effective mass or transport properties. Further quantitative analysis based on band structure calculations would be required to establish such relationships.[92]

3.7. Population analysis

Mulliken and Hirshfeld charge population analysis tabulated in Table S4 provides valuable insights into the electronic distribution and bonding character of A_3InX_6 (A = Rb, Cs; X = Cl, Br, I) defect perovskites materials. Mulliken analysis partitions electron density according to atomic orbital contributions and is therefore used here only to examine qualitative trends in charge transfer and bonding. However, it is well known that Mulliken population analysis has inherent limitations, particularly its sensitivity to the choice of basis set and its limited reliability in describing absolute atomic charges in extended solid-state systems. Therefore, in the present work, Mulliken analysis is employed strictly for qualitative interpretation of charge redistribution and bonding tendencies, and not for quantitative evaluation of absolute atomic charges. To complement this, Hirshfeld charge analysis is also employed to provide a comparatively more balanced description of electron-density distribution, although it is likewise considered only for qualitative interpretation.[93,94] Both analyses consistently indicate that the A-site cations (Rb, Cs) carry positive charge, reflecting their electropositive nature and supporting an overall ionic contribution to bonding within the lattice.

Hirshfeld charges follow the same trend but with smaller magnitudes, typically 0.14 to 0.42 e (Table S4), reflecting the method's more delocalized description. Indium atoms generally acquire positive Mulliken charges, *e.g.*, 0.74 e in Cs_3InCl_6, while Hirshfeld charges are lower, 0.42 e, highlighting their intermediate role between the electropositive A-site and electronegative halides. Conversely, halogen atoms (Cl, Br, I) display negative charges across all compounds, with the strongest Mulliken localization at −0.49 e (Cl in Cs_3InCl_6) and the weakest at −0.00 e (Br in Cs_3InBr_6), while Hirshfeld charges range from about −0.24 to −0.21 e, as shown in Table S4. A systematic trend is observed: moving from Cl → Br → I, the magnitude of negative halogen charge decreases, reflecting reduced electronegativity and increasing covalency. Likewise, substitution of Rb with Cs enhances charge transfer, as evidenced by larger positive Mulliken charges on Cs compared to Rb, consistent with the stronger interaction of Cs with halogens. Overall, Mulliken results tend to emphasize ionic contributions, whereas Hirshfeld analysis suggests a comparatively more delocalized electron distribution. These observations provide a qualitative indication of bonding characteristics, with relatively more ionic behavior in Rb–Cl systems and a tendency toward increased covalent contribution in Cs–I systems. It is important to emphasize that the present population analysis is intended only to describe general bonding trends. No direct conclusions regarding band-edge properties, carrier transport behavior, or device performance are drawn from these results. A more quantitative assessment of such properties would require advanced charge-partitioning methods (*e.g.*, DDEC or Bader analysis) or explicit calculations of effective mass and carrier mobility, which are beyond the scope of the present work.

4. Limitations

Although this work offers a comprehensive theoretical investigation of the structural, electronic, optical, and mechanical properties of A_3InX_6 defect-perovskites, several limitations should be acknowledged. First, all results are derived from density functional theory calculations using GGA-based exchange-correlation functionals, which are known to underestimate band-gap values; therefore, the absolute band gaps reported here should be interpreted qualitatively, while the observed trends with cation and anion substitution remain reliable. Second, the present study focuses exclusively on ideal, defect-free bulk crystals at zero temperature and ambient pressure. Effects arising from intrinsic point defects, grain boundaries, surface states, and finite-temperature lattice vibrations-which can significantly influence real material behavior-are not explicitly considered. Additionally, excitonic effects and many-body interactions are not included in the optical calculations, which may affect quantitative predictions of absorption and dielectric response. Finally, this work does not address thin-film growth, interfacial phenomena, charge-carrier transport, or device-level performance, which are essential aspects for practical optoelectronic applications. Consequently, while the present results provide valuable fundamental insights and identify promising compositions, experimental validation and more advanced theoretical treatments are required to fully assess the applicability of A_3InX_6 defect-perovskites in real devices.

5. Conclusion

In this work, first-principles density functional theory calculations were performed to investigate the structural, electronic, optical, and mechanical properties of lead-free alkali-indium halide defect perovskites A_3InX_6 (A = Rb, Cs; X = Cl, Br, I) for potential photovoltaic and optoelectronic applications. All compounds are found to be structurally stable within the adopted cubic framework, satisfying the Born mechanical stability criteria and exhibiting negative formation energies, indicating favorable thermodynamic feasibility. The calculated Goldschmidt tolerance factors confirm good geometric compatibility, with Cs-based systems showing slightly improved lattice matching due to the larger ionic radius. Electronic structure analysis reveals direct band gaps at the Γ-point, with systematic band-gap narrowing from Cl to I driven by increased halogen p-orbital contributions near the valence-band maximum. Iodide-based compositions demonstrate band gaps suitable for solar absorption, while chloride analogues remain promising for ultraviolet optoelectronic devices. Optical results indicate enhanced absorption coefficients, dielectric response, and optical conductivity in iodide-rich systems, confirming superior visible-light harvesting capability and tunable

optoelectronic performance through anion engineering. Mechanical analysis further suggests that all materials are ductile and relatively soft, with Cs- and I-containing compounds exhibiting greater deformability, advantageous for flexible devices. The predicted properties should therefore be interpreted as representative of an idealized cubic structural model that provides a consistent theoretical reference for future experimental validation, while acknowledging that alternative polymorphs may exist under different synthesis conditions.

Ethical statement

All procedures performed followed ethical standards.

Author contributions

Imtiaz Ahamed Apon, Md. Sakib Hasan, Rifat Rafiu, Md. Azizur Rahman: formal analysis, data curation, visualization, conceptualization, methodology, investigation, software, writing, review & editing – original draft. Mohamed Benghanem, Amnah Mohammed Alsuhaibani, Moamen S. Refat, Noureddine Elboughdiri: software, validation, visualization, resources, writing – review & editing.

Conflicts of interest

Authors declare that they have no competing interests.

Data availability

The datasets collected and analyzed during the current study are available upon request from the corresponding author. The corresponding author had full access to all data in the study and took responsibility for the integrity and accuracy of the data analysis.

Supplementary information (SI): additional data, figures, and equation details supporting this study. See DOI: https://doi.org/10.1039/d6ra00473c.

Acknowledgements

The researchers wish to extend their sincere gratitude to the Deanship of Scientific Research at the Islamic University of Madinah (KSA) for the support provided to the Post-Publishing Program. Princess Nourah bint Abdulrahman University researchers supporting project number (PNURSP2026R65), Princess Nourah bint Abdulrahman University, Riyadh, Saudi Arabia.

References

1 A. K. Jena, A. Kulkarni and T. Miyasaka, *Chem. Rev.*, 2019, **119**, 3036–3103.
2 A. Kojima, K. Teshima, Y. Shirai and T. Miyasaka, *J. Am. Chem. Soc.*, 2009, **131**, 6050–6051.
3 N.-G. Park, *Mater. Today*, 2015, **18**, 65–72.
4 L. Jonathan, L. J. Diguna, O. Samy, M. Muqoyyanah, S. Abu Bakar, M. D. Birowosuto and A. El Moutaouakil, *Polymers*, 2022, **14**, 1059.
5 M. A. Green, A. Ho-Baillie and H. J. Snaith, *Nat. Photonics*, 2014, **8**, 506–514.
6 S. D. Stranks, G. E. Eperon, G. Grancini, C. Menelaou, M. J. P. Alcocer, T. Leijtens, L. M. Herz, A. Petrozza and H. J. Snaith, *Science*, 2013, **342**, 341–344.
7 A. Babayigit, A. Ethirajan, M. Muller and B. Conings, *Nat. Mater.*, 2016, **15**, 247–251.
8 J. Huang, S. Tan, P. D. Lund and H. Zhou, *Energy Environ. Sci.*, 2017, **10**, 2284–2311.
9 F. Hao, C. C. Stoumpos, D. H. Cao, R. P. H. Chang and M. G. Kanatzidis, *Nat. Photonics*, 2014, **8**, 489–494.
10 T. Krishnamoorthy, H. Ding, C. Yan, W. Lin Leong, T. Baikie, Z. Zhang, M. Sherburne, S. Li, M. Asta, N. Mathews and S. G. Mhaisalkar, *J. Mater. Chem. A*, 2015, **3**, 23829–23832.
11 B.-W. Park, B. Philippe, X. Zhang, H. Rensmo, G. Boschloo and E. M. J. Johansson, *Adv. Mater.*, 2015, **27**, 6806–6813.
12 A. K. Baranwal, H. Masutani, H. Sugita, H. Kanda, S. Kanaya, N. Shibayama, Y. Sanehira, M. Ikegami, Y. Numata, K. Yamada, T. Miyasaka, T. Umeyama, H. Imahori and S. Ito, *Nano Converg.*, 2017, **4**, 26.
13 I. Turkevych, S. Kazaoui, E. Ito, T. Urano, K. Yamada, H. Tomiyasu, H. Yamagishi, M. Kondo and S. Aramaki, *ChemSusChem*, 2017, **10**, 3754–3759.
14 Y. Kim, Z. Yang, A. Jain, O. Voznyy, G.-H. Kim, M. Liu, L. N. Quan, F. P. García de Arquer, R. Comin, J. Z. Fan and E. H. Sargent, *Angew. Chem., Int. Ed.*, 2016, **55**, 9586–9590.
15 N. Pai, J. Lu, T. R. Gengenbach, A. Seeber, A. S. R. Chesman, L. Jiang, D. C. Senevirathna, P. C. Andrews, U. Bach, Y.-B. Cheng and A. N. Simonov, *Adv. Energy Mater.*, 2019, **9**, 1803396.
16 A. Kulkarni, A. K. Jena, M. Ikegami and T. Miyasaka, *Chem. Commun.*, 2019, **55**, 4031–4034.
17 Z. Shao, T. Le Mercier, M. B. Madec and T. Pauporté, *Mater. Lett.*, 2018, **221**, 135–138.
18 W. Zulhafizhazuan, K. Sobayel, S. Shafian, S. Sepeai and M. A. Ibrahim, *Interactions*, 2025, **246**, 29.
19 A. Kulkarni, F. Ünlü, N. Pant, J. Kaur, C. Bohr, A. K. Jena, S. Öz, M. Yanagida, Y. Shirai, M. Ikegami, K. Miyano, Y. Tachibana, S. Chakraborty, S. Mathur and T. Miyasaka, *Sol. RRL*, 2021, **5**, 2100077.
20 Y. Seo, S. R. Ha, S. Yoon, S. M. Jeong, H. Choi and D.-W. Kang, *J. Power Sources*, 2020, **453**, 227903.
21 T. I. Awan, S. Afsheen and S. Kausar, in *Thin Film Deposition Techniques: Thin Film Deposition Techniques and Its Applications in Different Fields*, ed. T. I. Awan, S. Afsheen and S. Kausar, Springer Nature, Singapore, 2025, pp. 241–278.
22 M. Li, M. Liu, F. Qi, F. R. Lin and A. K.-Y. Jen, *Chem. Rev.*, 2024, **124**, 2138–2204.
23 R. K. Sharme, M. Quijada, M. Terrones and M. M. Rana, *Materials*, 2024, **17**, 4559.
24 H. Arfin, A. S. Kshirsagar, J. Kaur, B. Mondal, Z. Xia, S. Chakraborty and A. Nag, *Chem. Mater.*, 2020, **32**, 10255–10267.

25 R. G. Parr, *Annu. Rev. Phys. Chem.*, 1983, **34**, 631–656.
26 S. J. Clark, M. D. Segall, C. J. Pickard, P. J. Hasnip, M. I. J. Probert, K. Refson and M. C. Payne, *Z. Kristallogr. Cryst. Mater.*, 2005, **220**, 567–570.
27 M. Ernzerhof and G. E. Scuseria, *J. Chem. Phys.*, 1999, **110**, 5029–5036.
28 J. P. Perdew, K. Burke and Y. Wang, *Phys. Rev. B: Condens. Matter Mater. Phys.*, 1996, **54**, 16533–16539.
29 J. E. Peralta, J. Heyd, G. E. Scuseria and R. L. Martin, *Phys. Rev. B: Condens. Matter Mater. Phys.*, 2006, **74**, 073101.
30 R. Sun, M. K. Y. Chan and G. Ceder, *Phys. Rev. B: Condens. Matter Mater. Phys.*, 2011, **83**, 235311.
31 G. Kresse and D. Joubert, *Phys. Rev. B: Condens. Matter Mater. Phys.*, 1999, **59**, 1758–1775.
32 R. J. Meier, *J. Mol. Struct. THEOCHEM*, 1999, **467**, 79–83.
33 P. Schwerdtfeger, *ChemPhysChem*, 2011, **12**, 3143–3155.
34 Y. Wang, P. Wisesa, A. Balasubramanian, S. Dwaraknath and T. Mueller, *Comput. Mater. Sci.*, 2021, **187**, 110100.
35 K. Choudhary and F. Tavazza, *Comput. Mater. Sci.*, 2019, **161**, 300–308.
36 M. G. Quezada-Aldaco, E. Delgado, D. E. Zazueta-Álvarez, V. J. Martínez-Gómez, H. Medrano-Roldán, P. G. Vázquez-Ortega, F. S. Hernández-Rodarte and D. Reyes-Jáquez, *Nanomaterials*, 2024, **14**(21), 1713.
37 M. I. Naher, M. A. Ali, M. M. Hossain, M. M. Uddin and S. H. Naqib, *Results Phys.*, 2023, **51**, 106742.
38 M. A. Jehangir, S. Rabhi, R. Makhloufi, A. I. Shimul, A. N. Khan, Y. I. Bouderbala, O. H. Alsalmi, S. Sadaf and M. W. Alam, *RSC Adv.*, 2026, **16**, 13083–13102.
39 X. Xian, D. Wang, G. Xu, W. Luo, S. Yuan, F. Chen, Y. Pu, F. Qi, N. Zhang, X. Tang and Q. Huang, *ACS Sustain. Chem. Eng.*, 2026, **14**, 5911–5921.
40 J. D. Majher, M. B. Gray, T. Liu, N. P. Holzapfel and P. M. Woodward, *Inorg. Chem.*, 2020, **59**, 14478–14485.
41 R. Rafiu, Md. S. Hasan, Md. A. Rahman, I. A. Apon, K. Kriaa, M. Benghanem, S. AlFaify and N. Elboughdiri, *RSC Adv.*, 2026, **16**, 7803–7829.
42 M. J. Islam and R. Amin, *Mater. Res. Express*, 2026, **13**, 015902.
43 S. M. Alqahtani, A. Q. Alsayoud and F. H. Alharbi, *RSC Adv.*, 2023, **13**, 9026–9032.
44 W. Travis, E. N. K. Glover, H. Bronstein, D. O. Scanlon and R. G. Palgrave, *Chem. Sci.*, 2016, **7**, 4548–4556.
45 C. J. Bartel, C. Sutton, B. R. Goldsmith, R. Ouyang, C. B. Musgrave, L. M. Ghiringhelli and M. Scheffler, *Sci. Adv.*, 2019, **5**, eaav0693.
46 V. M. Goldschmidt, *Naturwissenschaften*, 1926, **14**, 477–485.
47 R. Ubic and G. Subodh, *J. Alloys Compd.*, 2009, **488**, 374–379.
48 W. S. Kamoru, M. B. Haider, B. U. Haq, S. H. Aleithan, A. M. Alsharari, S. Ullah and K. Alam, *Results Phys.*, 2024, **57**, 107387.
49 J. Epp, in *Materials Characterization Using Nondestructive Evaluation (NDE) Methods*, ed. G. Hübschen, I. Altpeter, R. Tschuncky and H.-G. Herrmann, Woodhead Publishing, 2016, pp. 81–124.
50 Materials Project, https://next-gen.materialsproject.org/materials/mp-1110693?formula=Rb3InCl6, accessed April 9, 2026.
51 R. Rafiu, M. S. Hasan Saikot, I. A. Apon, I. Boukhris, A. El-Rayyes, M. T. Khan, Q. Mohsen and M. A. Rahman, *J. Comput. Chem.*, 2025, **46**, e70221.
52 M. S. H. Saikot, R. Rafiu, M. Azizur Rahman, I. Ahamed Apon, A. El-Rayyes, M. Taukeer Khan, Z. Ahmad and M. Shkir, *New J. Chem.*, 2025, **49**, 16340–16369.
53 L. He, F. Liu, G. Hautier, M. J. T. Oliveira, M. A. L. Marques, F. D. Vila, J. J. Rehr, G.-M. Rignanese and A. Zhou, *Phys. Rev. B: Condens. Matter Mater. Phys.*, 2014, **89**, 064305.
54 S. Saroar, S. Sultana, S. S. Nishat, Q. S. Hossain, M. N. I. Khan, D. Islam, U. S. Akhtar, M. Shahriar Bashar, S. Jahan, K. S. Hossain and I. Ahmed, *ACS Omega*, 2024, **9**, 36314–36325.
55 Y. Nassah, A. Benmakhlouf and E. O. Remache, *The Islamic University Journal of Applied Sciences*, 2026, 113–122.
56 I. Garoui, N. Weslati, I. Chaabane, N. A. Alghamdi, M. Tliha and A. Oueslati, *Opt. Mater.*, 2026, **169**, 117651.
57 J. S. Manser, J. A. Christians and P. V. Kamat, *Chem. Rev.*, 2016, **116**, 12956–13008.
58 M. Saiduzzaman, T. Ahmed, K. M. Hossain, A. Biswas, S. K. Mitro, A. Sultana, M. S. Alam and S. Ahmad, *Mater. Today Commun.*, 2023, **34**, 105188.
59 T. Zdanowicz, T. Rodziewicz and M. Zabkowska-Waclawek, *Sol. Energy Mater. Sol. Cells*, 2005, **87**, 757–769.
60 K. W. Guji, T. A. Geleta, N. Bouri and V. J. Ramirez Rivera, *Nanoscale Adv.*, 2024, **6**, 4479–4491.
61 M. A. Hossain, A. Hosen, H. A. Abdulhussein, A. A. Mousa, M. M. Hasan, I. A. Ovi, M. R. Islam, R. K. Pingak and M. S. Abu-Jafar, *Results Eng.*, 2024, **24**, 103340.
62 K. Yang, Y. Dai, B. Huang and M.-H. Whangbo, *Chem. Mater.*, 2008, **20**, 6528–6534.
63 M. Y. Khan, M. A. Jehangir, N. Israr, A. Hassan, U. Younis, J. Khan, M. Khan, A. Khan and A. Al Souwaileh, *Phys. B Condens. Matter*, 2025, **707**, 417150.
64 M. A. Jehangir, M. Y. Khan, M. Noman, I. E. Lee, Q. Wali, T. Usman, Y. Mu and A. A. Souwaileh, *RSC Adv.*, 2025, **15**, 33708–33725.
65 I. A. Apon, M. A. Hossain, R. Rafiu, M. S. Hasan Saikot, M. A. Rahman, J. R. Rajabathar, I. Boukhris, H. Albalawi, K. Kriaa and N. Elboughdiri, *Phys. B Condens. Matter*, 2025, **717**, 417836.
66 S. Poncé, W. Li, S. Reichardt and F. Giustino, *Rep. Prog. Phys.*, 2020, **83**, 036501.
67 M. A. Rahman, R. Rafiu, I. A. Apon, M. S. Hasan Saikot, I. A. Ovi, N. Elboughdiri, M. Benghanem, S. AlFaify, I. M. Ashraf and H. Albalawi, *Mater. Chem. Phys.*, 2026, **349**, 131777.
68 R. K. Pingak, Z. S. Ngara, A. Z. Johannes, M. Bukit and J. L. Tanesib, *Comput. Condens. Matter*, 2024, **40**, e00928.
69 M. Hilal, B. Rashid, S. H. Khan and A. Khan, *Mater. Chem. Phys.*, 2016, **184**, 41–48.
70 R. Rafiu, K. Kriaa, M. S. H. Saikot, M. A. Rahman, I. A. Apon, N. Sfina, M. T. Khan, N. Elboughdiri, S. AlFaify and I. A. Talukder, *RSC Adv.*, 2025, **15**, 44711–44748.

71 X. D. He, K. E. Torrance, F. X. Sillion and D. P. Greenberg, *SIGGRAPH Computer Graphics*, 1991, **25**, 175–186.
72 S. Ando, *J. Photopolym. Sci. Technol.*, 2006, **19**, 351–360.
73 M. Vuori, A. Penttilä, K. Muinonen, H. Suhonen and J. Jääskeläinen, *J. Quant. Spectrosc. Radiat. Transf.*, 2025, **331**, 109269.
74 J. Wu, Z. T. Xie, Y. Sha, H. Y. Fu and Q. Li, in *Frontiers in Optics/Laser Science*, Optica Publishing Group, Washington, DC, 2020, p. JTu1A.34.
75 C. M. Sorensen, J. B. Maughan and H. Moosmüller, *J. Quant. Spectrosc. Radiat. Transf.*, 2019, **226**, 81–86.
76 R. F. Egerton, *Rep. Prog. Phys.*, 2008, **72**, 016502.
77 A. P. Sutton, in *Physics of Elasticity and Crystal Defects*, ed. A. P. Sutton, Oxford University Press, 2020.
78 M. Born and K. Huang, *Dynamical Theory of Crystal Lattices*, Oxford University Press, New York, NY, 1996.
79 J. Gao, Q.-J. Liu and B. Tang, *J. Appl. Phys.*, 2023, **133**, 135901.
80 T. A. Saleh, in *Surface Science of Adsorbents and Nanoadsorbents*, ed. T. A. Saleh, Elsevier, 2022, vol. 34, pp. 233–263.
81 Z. Duan, L. Su, Y. Duan, L. Ma, A. Yang, L. Su, M. Li and Y. He, *Ceram. Int.*, 2025, **51**, 13634–13645.
82 D. H. Chung and W. R. Buessem, *J. Appl. Phys.*, 1968, **39**, 2777–2782.
83 P. Yang, G. Boer, F. Snow, A. Williamson, S. Cheeseman, R. M. Samarasinghe, A. Rifai, A. Priyam, R. Elnathan, R. Guijt, A. Quigley, R. Kaspa, D. R. Nisbet and R. J. Williams, *Chem. Eng. J.*, 2025, **505**, 159295.
84 R. Rafiu, K. Kriaa, M. A. Rahman, I. A. Apon, S. AlFaify, C. Maatki, M. S. Hasan and N. Elboughdiri, *Eur. Phys. J. Plus*, 2026, **141**, 32.
85 Y. Tian, B. Xu and Z. Zhao, *Int. J. Refract. Met. Hard Mater.*, 2012, **33**, 93–106.
86 M. N. Sousa, N. E. Luiz, D. C. de Oliveira, M. A. d. S. Barrozo and Á. R. Machado, *Mater. Sci. Technol.*, 2012, **28**, 220–226.
87 M. Born, *Math. Proc. Camb. Phil. Soc.*, 1940, **36**, 160–172.
88 H. Ledbetter and A. Migliori, *J. Appl. Phys.*, 2006, **100**, 063516.
89 F. Najrin, M. A. Sarker, B. Neher and M. M. R. Bhuiyan, *Results Mater.*, 2024, **23**, 100610.
90 I. A. Apon, M. R. Hasan, R. Rafiu, R. Kawsar, M. S. Hasan Saikot, M. A. Hossain, M. A. Rahman, K. Kriaa, N. Elboughdiri, Q. Mohsen, M. T. Khan and A. A. Alshihri, *J. Inorg. Organomet. Polym. Mater.*, 2026, **36**, 1377–1400.
91 E. Bisong, in *Building Machine Learning and Deep Learning Models on Google Cloud Platform*, Apress, Berkeley, CA, 2019, pp. 59–64.
92 R. Rafiu, K. Kriaa, M. S. H. Saikot, M. A. Rahman, I. A. Apon, N. Sfina, M. T. Khan, N. Elboughdiri, S. AlFaify and I. A. Talukder, *RSC Adv.*, 2025, **15**, 44711–44748.
93 R. S. Mulliken, *J. Chem. Phys.*, 1955, **23**, 1833–1840.
94 F. L. Hirshfeld, *Theor. Chim. Acta*, 1977, **44**, 129–138.